Research Square

Preprints are preliminary reports that have not undergone peer review.
They should not be considered conclusive, used to inform clinical practice,
or referenced by the media as validated information.

Steady, Quasi-Periodic, and Chaotic Regimes of Natural Convection Around a Heated Cylinder in a Square Cavity

Mannu Yadav
National Institute of Technology Sikkim
Anil Lal Sadasivan
anillal65@gmail.com

National Institute of Technology Sikkim

Research Article

Keywords: Natural convection, Square cavity with heated cylinder, Finite element method, Regime transition and chaos, Energy spectral density, Poincare section

Posted Date: July 7th, 2026

DOI: https://doi.org/10.21203/rs.3.rs-10168816/v1

License: This work is licensed under a Creative Commons Attribution 4.0 International License.
Read Full License

Additional Declarations: No competing interests reported.

Steady, Quasi-Periodic, and Chaotic Regimes of Natural Convection Around a Heated Cylinder in a Square Cavity

Mannu Yadav[1] and Anil Lal Sadasivan[1*]

[1]Department of Mechanical Engineering, National Institute of Technology Sikkim, Ravangla, Namchi, 737139, Sikkim, India.

*Corresponding author(s). E-mail(s): anillal65@gmail.com;
Contributing authors: mannuyadavh@gmail.com;

Abstract

This article reports a numerical study of buoyancy-driven air flow ($\boldsymbol{Pr = 0.71}$) in a cold square cavity that holds a heated circular cylinder of radius $\boldsymbol{R = 0.2L}$ at its centre. Eight Rayleigh numbers were covered, from $\mathbf{10^4}$ to $\mathbf{5 \times 10^7}$, using a pressure-based finite element solver on a body-conforming mesh that keeps the unsteady terms and places no symmetry condition on the flow, so that asymmetric modes are free to grow on their own. Three distinct regimes emerged from this study. The flow stays steady up to $\boldsymbol{Ra \approx 5 \times 10^6}$, with two mirror-image recirculation cells around the cylinder and a single plume rising from the top of the cylinder to the cold top wall. Tracking the standard deviation of the cylinder-averaged Nusselt number locates the onset of unsteadiness in the range $\mathbf{5 \times 10^6 < Ra_c < 7.5 \times 10^6}$. Past this point the flow reaches chaos along the Ruelle-Takens-Newhouse route, beginning as a single-frequency limit cycle at $\boldsymbol{Ra = 7.5 \times 10^6}$, turning quasi-periodic on a two-torus at $\boldsymbol{Ra = 10^7}$, and ending in a broad-band strange attractor at $\boldsymbol{Ra = 5 \times 10^7}$, with energy spectra and Poincaré maps recorded at eleven probes confirming each stage. The disorder first sets in at the plume above the cylinder and reaches the lower stratified pool only at the highest Rayleigh number. A single power law, $\boldsymbol{\overline{Nu}_{cyl} = 0.764\, Ra^{0.226}}$, fits all eight time-averaged cylinder Nusselt numbers to within **6%**. Across the whole range the top wall absorbs close to **55%** of the heat reaching the walls, while the bottom wall accounts for less than **2%**, a direct effect of the strengthening thermal stratification in the lower cavity.

Keywords: Natural convection, Square cavity with heated cylinder, Finite element method, Regime transition and chaos, Energy spectral density, Poincaré section

1 Introduction

Natural convection inside a square cavity with a heated cylinder is one of the most important configurations for the study of buoyancy-driven flow and heat transfer in confined geometries. In forced convection an external agent drives the fluid, but natural convection relies entirely on density differences created by temperature gradients to set the fluid in motion. When this motion is enclosed by solid walls, the boundaries restrict the growth of convective currents, generate recirculation zones, and force a balance among buoyancy, inertia, and viscous resistance. The problem is therefore physically rich and, at the same time, of clear practical relevance. Typical applications include passive cooling of miniaturized electronic devices, emergency heat removal in nuclear reactors, temperature control of chemical reactors, and the prediction of urban thermal plumes that guide building design for natural ventilation and indoor air quality [7, 20, 24].

For several decades the differentially heated square cavity has served as the standard benchmark for buoyancy-driven flow, mainly because its geometry is simple and its thermal boundary conditions leave no ambiguity. The early study of De Vahl Davis [14] produced reliable reference solutions for steady laminar natural convection of air in a Boussinesq fluid for Rayleigh numbers between 10^3 and 10^6. These results were obtained on systematically refined finite-difference grids and became a standard reference. Hortmann et al. [21] and Le Quéré [30] later extended the range up to $Ra = 10^8$ using high-accuracy spectral methods.

Several subsequent work has confirmed that the Rayleigh number is the most dominant parameter controlling both the flow pattern and the strength of heat transport [5, 36, 41]. At low Ra the temperature field is nearly linear and heat moves across the cavity almost entirely by conduction. Once Ra grows beyond roughly 10^3, buoyancy is strong enough to overcome viscous resistance and a steady convection cell develops, which significantly boosts the heat transfer rate. The mean Nusselt number then rises with Ra following well-known power-law correlations. At sufficiently high Ra, thin thermal and momentum boundary layers form along the heated walls, the bulk of the cavity becomes thermally stratified, and the flow eventually loses its steady character. Direct numerical simulations and large-eddy simulations by Versteegh and Nieuwstadt [46] and later by Trias et al. [45] showed that this loss of steadiness manifests itself as oscillating thermal plumes, vortex interactions, and other unsteady structures that further enhance the wall heat transfer.

Oztop et al. [35] studied steady laminar convection around a heated cylinder placed at the centre of cold square cavity and showed that even a modest cylinder strongly reorganizes the flow. Subsequent studies by Mahmoodi [31], Sun et al. [43], and Kim et al. [26] examined the role of cylinder size, position, and boundary-layer interaction, and reported clear changes in flow symmetry and in the local Nusselt number distribution. When the cylinder is moved off the centreline, the left-right symmetry of the flow breaks and the heat transfer along the hot and cold walls becomes unequal.

Another important parameter that influences the heat transfer is the size of the cylinder. Small cylinders behave as compact heat sources that drive a single dominant recirculation loop, whereas large cylinders block the gap between the cylinder surface and the cavity walls and force the flow to split into several counter-rotating cells.

This change in flow topology has a direct and non-monotonic effect on the mean Nusselt number, with several studies reporting a local minimum in heat transfer at intermediate cylinder radii before convection recovers at larger sizes [26, 43]. These results show that the thermal performance of the system is very sensitive to geometric parameters even in apparently simple arrangements.

For higher Rayleigh numbers, Wang et al. [47] provided early evidence of time-dependent behaviour around an enclosed cylinder. Their simulations showed that the flow remains steady at low and moderate Rayleigh numbers, with a stable plume and two symmetric recirculation cells. Above $Ra \approx 10^6$, however, the thermal plume begins to oscillate periodically and buoyant thermals detach from the top of the cylinder at a well-defined frequency that scales with Ra in a manner consistent with a Hopf-type instability. The onset of this unsteadiness is sharp rather than gradual, appearing with finite amplitude once buoyancy exceeds a critical threshold. Their time-averaged fields retained the bilateral symmetry of the configuration even in the unsteady regime, since over a long record the flow visits every state and its mirror image equally often; the instantaneous snapshots, by contrast, were asymmetric. The study was confined to a limited set of geometries and Rayleigh numbers, and the dependence of the critical Rayleigh number on cylinder size and position was left open.

A systematic study was carried out by Dutta et al. [17]. They developed a streamfunction-velocity (ψ-v) framework combined with a fourth-order compact finite difference scheme to study natural convection around a heated circular cylinder of radius $R = 0.2L$ placed inside a cold square enclosure. The computations were carried out on non-uniform body-fitted grids without co-ordinate transformation which eliminates the need for immersed boundary interpolation. The Rayleigh number was varied from 10^3 to 10^7 at $Pr = 0.71$, and the cylinder was displaced along the vertical centre line over $-0.25L \leq \delta \leq 0.25L$. For the centrally placed cylinder ($\delta = 0$), the flow reached a steady state at every Ra, with two symmetric counter-rotating cells, a rising thermal plume above the cylinder, and corner vortices at the bottom wall that appeared at $Ra = 10^6$ and grew with increasing Ra. Off-centre placement produced richer flow topologies: the single plume split into multiple ascending plumes with secondary vortices on the cylinder cap, and at $Ra = 10^7$ steady convergence was limited to $0.05 \leq \delta \leq 0.18$. The surface-averaged Nusselt numbers on the four enclosure walls and on the cylinder were reported as functions of both Ra and δ.

Despite a systematic study the framework of Dutta et al. [17] leaves several unanswered questions. The analysis is restricted to steady-state solutions and therefore cannot capture time-dependent phenomena such as plume oscillation, vortex interaction, and transient fluctuations of the heat transfer rate, all of which are expected at higher Ra. The transition from steady to unsteady convection, which fundamentally changes both the structure of the flow and the character of the heat transfer, was not addressed. In addition, the stream function on the cylinder surface was set to zero, which artificially enforces left-right symmetry about the vertical centre line and prevents the natural emergence of asymmetric flow modes. This constraint filters out any symmetry-breaking instability of the problem and may produce solutions that are numerically stable but physically incomplete.

The published literature, while substantial, therefore leaves a meaningful gap in the understanding of unsteady natural convection around an enclosed cylinder. Steady-state studies cannot reveal the time-dependent phenomena that become important as Ra grows. Only the few unsteady investigations that exist [47] are narrow in their parametric scope and do not trace the full sequence of states between the steady laminar limit and developed time-periodic regime. The artificial symmetry imposed in earlier work [17] suppresses asymmetric modes that may emerge naturally at higher Ra and may overestimate the critical Rayleigh number for the onset of unsteadiness. As a consequence, the value of this critical Rayleigh number, the sequence of regimes that follow it, and their effect on local and average Nusselt numbers remain unresolved for an air-filled cavity ($Pr = 0.71$) with a centrally heated cylinder. The present study is motivated directly by these gap areas.

This work investigates unsteady natural convection around a heated circular cylinder placed at the centre of a square cavity for Rayleigh number that span the steady, transitional, and unsteady regimes. The simulations are time-dependent: the unsteady terms in the governing equations are kept, and no symmetry constraint is enforced, so any asymmetric mode that the physics admits is free to grow on its own. The numerical scheme is a pressure-based finite element method on a body-conforming mesh, chosen because the fine-scale structures near the cylinder and inside the thermal plume need to be resolved cleanly once the flow loses its steady character.

The three primary objectives of this study are: First, to bracket the critical Rayleigh number at which the steady state breaks. Second, to identify, one at a time, the unsteady regimes that follow it. Third, to find the influence of each regime on the local and average Nusselt numbers, both around the cylinder and on the cavity walls. The results are expected to deepen the understanding of enclosed convection systems and to provide reliable data for the configuration where both internal geometry and unsteady dynamics act together.

This article is organized as follows. Section 2 presents the physical model and the governing equations, with the cavity geometry described first and then the Navier-Stokes and energy equations for the fluid motion and heat transfer. Section 3 explains the numerical method, the body-conforming grid construction and the full solution procedure. Section 4 validates the in-house FORTRAN code against the standard benchmark of De Vahl Davis [14]. Section 5 presents the results in four parts: the grid independence study in Section 5.1; the steady regime ($10^4 \leq Ra \leq 5 \times 10^6$) in Section 5.2; a regime-transition analysis driven by the time history of the cylinder-averaged Nusselt number at all eight Rayleigh numbers in Section 5.3, where the critical Rayleigh number for the onset of unsteadiness is found; and the unsteady regime ($Ra \geq 7.5 \times 10^6$) in Section 5.4, treated through the instantaneous and time-averaged fields, the heat transfer, the energy spectral densities, and the Poincaré maps recorded at the probe points. Section 6 draws the main findings together.

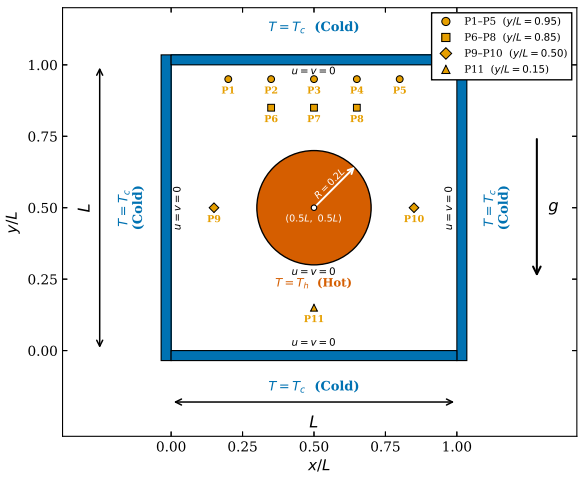


Fig. 1: Schematic of natural convection around a heated cylinder in a square cavity, with the locations of the eleven probes P1–P11 used to record time signals.

2 Physical model and governing equations

2.1 Geometric configuration and boundary conditions

The problem to be investigated is the two-dimensional natural convection of air confined between a heated circular cylinder and the walls of a square enclosure. A schematic of the configuration, together with the positions of the probes used to record time signals of the flow variables, is shown in Fig. 1. The cavity is a square of side L aligned with a Cartesian (x, y) frame whose origin is placed at the lower-left corner, so that the enclosure occupies $0 \le x/L, y/L \le 1$. Gravity acts in the negative y-direction, $\mathbf{g} = -g\,\hat{\mathbf{e}}_y$. A circular cylinder of radius $R = 0.2\,L$ is placed concentrically at the geometric centre of the cavity, $(x_c, y_c) = (0.5\,L, 0.5\,L)$, leaving a minimum clearance of $0.3\,L$ between the cylinder surface and each of the four walls.

The working fluid is air, treated as a Newtonian incompressible continuum under the Boussinesq approximation. Density variations enter the momentum balance only through the buoyancy term, while all other thermophysical properties are held constant. Thermally, the cylinder surface is kept at a uniform hot temperature T_h and the four walls of the cavity at a uniform cold temperature T_c, with $T_h > T_c$ so that buoyancy drives the fluid upward from the cylinder. Kinematically, the no-slip and impermeability conditions $u = v = 0$ are imposed on the cylinder surface and on the four walls, which is consistent with the assumption of a viscous fluid in contact with rigid stationary boundaries. Radiative exchange between the cylinder and the walls is neglected throughout, so that heat is transported only by conduction and convection through the fluid and by the buoyancy-driven motion that this conduction and convection sets up. The flow regime is controlled by the Rayleigh number Ra and the Prandtl number Pr is kept constant at 0.71. Ra is varied to follow the transition from the steady regime, through a periodic oscillatory state, into a chaotic regime.

In the post critical regime, time signals of velocity and temperature are recorded at eleven probe points distributed across four horizontal lines so that the spectral and phase space analyses are not biased toward a single part of the flow. Five probes (P1–P5) lie along $y/L = 0.95$ at $x/L = 0.2, 0.35, 0.5, 0.65, 0.8$, sampling the flow immediately below the cold top wall where the plume impinges and the shear is strongest. Three further probes (P6–P8) lie along $y/L = 0.85$ at $x/L = 0.35, 0.5, 0.65$ and capture the region between the plume head and the upper wall boundary layer. Two probes (P9 and P10) sit on the horizontal mid-line $y/L = 0.5$ on either side of the cylinder, at $x/L = 0.15$ and $x/L = 0.85$, so that the side wall descending jets are resolved. Probe (P11) is placed at $(x/L, y/L) = (0.5, 0.15)$ below the cylinder to record the activity of the lower stratified pool and of the bottom corner eddies.

2.2 Mathematical formulation

The fluid flow and the heat transfer inside the cavity are described by the unsteady two-dimensional Navier-Stokes equations coupled with the energy equation. In dimensional primitive variable form the governing equations under the Boussinesq approximation are

$$\frac{\partial U}{\partial X} + \frac{\partial V}{\partial Y} = 0, \tag{1}$$

$$\frac{\partial U}{\partial t'} + U\frac{\partial U}{\partial X} + V\frac{\partial U}{\partial Y} = -\frac{1}{\rho}\frac{\partial P}{\partial X} + \nu\,\nabla^2 U, \tag{2}$$

$$\frac{\partial V}{\partial t'} + U\frac{\partial V}{\partial X} + V\frac{\partial V}{\partial Y} = -\frac{1}{\rho}\frac{\partial P}{\partial Y} + \nu\,\nabla^2 V + g\beta\,(T - T_0)\,, \tag{3}$$

$$\frac{\partial T}{\partial t'} + U\frac{\partial T}{\partial X} + V\frac{\partial T}{\partial Y} = \alpha\left[\frac{\partial^2 T}{\partial X^2} + \frac{\partial^2 T}{\partial Y^2}\right], \tag{4}$$

where U and V are the velocity components in the X- and Y-directions, P is the pressure, T is the temperature, ρ is the fluid density, ν is the kinematic viscosity, β is the volumetric thermal expansion coefficient, and α is the thermal diffusivity. The last term in Eqn. (3) is the buoyancy force that drives natural convection inside the enclosure.

To make the analysis general and to reduce the number of independent parameters, the following dimensionless variables are introduced

$$x = \frac{X}{L}, \quad y = \frac{Y}{L}, \quad u = \frac{U}{U_0}, \quad v = \frac{V}{U_0}, \quad t = \frac{t'\,U_0}{L}, \quad p = \frac{P}{\rho\,U_0^2}, \quad \theta = \frac{T - T_c}{T_h - T_c}, \tag{5}$$

where L is the cavity side length, U_0 is the reference velocity, and T_h and T_c are the hot and cold wall temperatures. Substituting Eqn. (5) into Eqns. (1)-(4) gives the dimensionless governing equations

$$\frac{\partial u}{\partial x} + \frac{\partial v}{\partial y} = 0, \tag{6}$$

$$\frac{\partial u}{\partial t} + u\frac{\partial u}{\partial x} + v\frac{\partial u}{\partial y} = -\frac{\partial p}{\partial x} + Pr\,\nabla^2 u, \tag{7}$$

$$\frac{\partial v}{\partial t} + u\frac{\partial v}{\partial x} + v\frac{\partial v}{\partial y} = -\frac{\partial p}{\partial y} + Pr\,\nabla^2 v + Ra\,Pr\,\theta, \tag{8}$$

$$\frac{\partial \theta}{\partial t} + u\frac{\partial \theta}{\partial x} + v\frac{\partial \theta}{\partial y} = \frac{\partial^2 \theta}{\partial x^2} + \frac{\partial^2 \theta}{\partial y^2}. \tag{9}$$

The two governing dimensionless parameters, the Rayleigh number Ra and the Prandtl number Pr, are defined as

$$Ra = \frac{g\,\beta\,\Delta T\,L^3}{\nu\,\alpha}, \qquad Pr = \frac{\nu}{\alpha}. \tag{10}$$

The Rayleigh number measures the relative strength of buoyancy and viscous forces and controls the onset and the intensity of natural convection. The Prandtl number compares the rates of momentum and thermal diffusion in the fluid.

The pressure can be removed from the system by recasting the equations in vorticity-stream-function form. The dimensionless vorticity ω and the stream function ψ are defined by

$$\omega = \frac{\partial v}{\partial x} - \frac{\partial u}{\partial y}, \tag{11}$$

$$u = \frac{\partial \psi}{\partial y}, \qquad v = -\frac{\partial \psi}{\partial x}, \tag{12}$$

$$\nabla^2 \psi = -\omega. \tag{13}$$

The definition in Eqn. (12) satisfies the continuity equation (6) identically, and Eqn. (13) links the stream function to the vorticity through a Poisson equation. The present numerical algorithm, however, is built on the primitive variable form of Eqns. (6)-(9); the stream-function is reported here only for the visualization of the flow patterns presented in Section 5.

3 Numerical methodology

The numerical machinery used to solve the governing equations of Section 2.2 on the geometry described in Section 2.1 is discussed in this section. The work flow is split into two parts. First, a body conforming mesh is built on top of a Cartesian background grid through a ray cast projection step followed by a harmonic smoothing step (Section 3.1). Second, the dimensionless governing equations are advanced in time on the resulting mesh by a pressure-based fractional-step finite element solver (Section 3.2).

3.1 Grid generation

We have considered a computational domain Ω covered by a uniform Cartesian background grid $\mathcal{G}$ with spacings Δx and Δy that surrounds a set of immersed bodies. Each body is described by a closed piecewise-linear boundary curve $\Gamma_i = \{\mathbf{x}_{ik}\}_{k=1}^{N_i}$, with $i = 1, 2, \ldots, n_{ib}$, where n_{ib} is the total number of immersed bodies and N_i is the number of vertices that describe Γ_i. The construction is restricted to simply connected convex bodies and the extension to non-convex bodies follows the same algorithm with a separate interior point test which will be considered in future work.

To make the detection of intersection points fast and to limit the work needed to compute node splittings and boundary displacements, the axis aligned bounding box of each body is computed first,

$$\mathcal{B}_i = [x_{\min}^{(i)},\, x_{\max}^{(i)}] \times [y_{\min}^{(i)},\, y_{\max}^{(i)}]. \tag{14}$$

All operations associated with Γ_i are then confined to the $\mathcal{O}(\sqrt{N})$ nodes of $\mathcal{G}$ that fall inside $\mathcal{B}_i$, instead of the full N nodes of the grid.

Definition 1 (Interior node) A node $\mathbf{x}_g = (x_g, y_g) \in \mathcal{B}_i$ is said to be *interior* to Γ_i if, for every oriented segment $(\mathbf{x}_{ik}, \mathbf{x}_{i,k+1})$ of a counter-clockwise parametrization of Γ_i,

$$(y_g - y_{ik})(x_{i,k+1} - x_{ik}) \geq (y_{i,k+1} - y_{ik})(x_g - x_{ik}). \tag{15}$$

A node that fails this inequality for at least one segment is declared *exterior*. A binary tag $\texttt{ntype}(\mathbf{x}_g) \in \{0, i\}$ stores the result, with the value i indicating an interior node of the i^{th} body.

A node is called *boundary-adjacent* with respect to Γ_i when $\texttt{ntype}(\mathbf{x}_g) = i$ and at least one of its four cardinal neighbours (west, south, east or north) is exterior. From each such node, four unit rays $\hat{\mathbf{e}}_r$, $r \in \{1, 2, 3, 4\}$, are cast along the $-x$, $-y$, $+x$ and $+y$ directions respectively. A ray is considered *active* only if its cardinal neighbour lies in the exterior region. The intersection of an active ray with Γ_i is found by locating the unique segment $(\mathbf{x}_{ik}, \mathbf{x}_{i,k+1})$ that crosses the ray and by solving a one parameter linear interpolation along that segment. For a ray fired in direction r from $\mathbf{x}_g$, the normalized distance to the boundary is

$$\alpha_r = \frac{\left| \mathbf{x}_r^{\text{int}} - \mathbf{x}_g \right|}{h_r}, \qquad h_r \in \{\Delta x, \Delta y\}, \tag{16}$$

with $h_r = \Delta x$ for $r \in \{1, 3\}$ and $h_r = \Delta y$ for $r \in \{2, 4\}$. The candidate projection associated with the r^{th} ray is

$$\mathbf{x}_g^{(r)} = \mathbf{x}_g + \alpha_r\, h_r\, \hat{\mathbf{e}}_r, \qquad \alpha_r \in [0, 1]. \tag{17}$$

The admissibility test $\alpha_r \leq 1$ rejects spurious intersections that fall beyond the neighbouring cell and protects the algorithm from false hits at corners of non-smooth boundaries.

Let $\nu(\mathbf{x}_g) \in \{1, 2, 3\}$ be the number of rays that return an admissible intersection at the boundary adjacent node $\mathbf{x}_g$. When $\nu = 1$, the node is simply moved to its

unique projection on Γ_i. When $\nu \geq 2$, the node has more than one geometrically distinct projection on Γ_i and is therefore *split*: one copy of the node is sent to each projection and the multiplicity is recorded in a counter that is consulted later during cell reconstruction. The displacement vector associated with each projection is

$$\mathbf{d}_{i,k}^{(r)} = \mathbf{x}_{ik} - \mathbf{x}_g, \tag{18}$$

where $\mathbf{x}_{ik}$ is the point of Γ_i matched to the r^{th} ray, and the index k runs over all boundary-adjacent nodes associated with Γ_i.

Remark 1 (Admissible ray combinations) Under the convexity assumption stated at the beginning of this section, the admissible ray combinations at a split node are reduced to $\{1, 4\}$, $\{3, 4\}$, $\{1, 2\}$ and $\{2, 3\}$ for $\nu = 2$, and to $\{1, 2, 3\}$ or $\{2, 3, 4\}$ for $\nu = 3$. Any other combination signals a non-convex feature at sub-grid scale and is flagged by the implementation.

The set of candidate projections returned by the ray-cast step is in general not uniformly distributed along Γ_i. Where the boundary is nearly aligned with the grid, the projections cluster, whereas in regions inclined at about 45° to the grid the projections remain sparse. To restore an even spacing, Γ_i is parametrized by its cumulative arc length s and the projections are sorted in increasing s. With L_i the perimeter of Γ_i and N_i^{proj} the number of projected points on it, the target spacing is

$$\Delta s^* = \frac{L_i}{N_i^{\text{proj}}}. \tag{19}$$

A further local correction is applied to avoid degenerate cells. For three consecutive sorted projections, let Δs^- and Δs^+ be the arc-length gaps on either side of the central point and define

$$\rho = \frac{\max(\Delta s^-, \Delta s^+)}{\Delta s^- + \Delta s^+}. \tag{20}$$

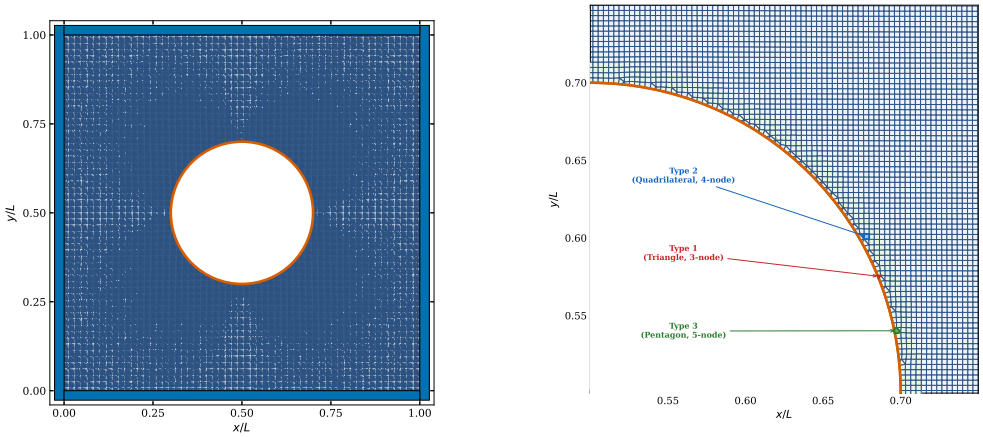
When ρ exceeds a threshold ρ^* (we take $\rho^* = 0.7$ everywhere in this work), the central projection is nudged toward its more distant neighbour by a fraction $(\rho - \rho^*)$, which brings the ratio back to ρ^*. This step caps the aspect ratio of the boundary adjacent cells at roughly 1:3 and prevents two adjacent edges of Γ_i from collapsing.

The displacements obtained so far are defined only at the boundary adjacent nodes. To make the mesh smooth around the immersed surface, they are propagated into the interior of the domain by solving the harmonic problem

$$\nabla^2 \mathbf{d} = \mathbf{0}, \qquad \mathbf{d}\big|_{\Gamma_i} = \mathbf{d}_i, \qquad \mathbf{d}\big|_{\partial\Omega} = \mathbf{0}, \qquad \mathbf{d}\big|_{\Gamma_j} = \mathbf{0}, \tag{21}$$

where $\partial\Omega$ denotes the outer walls of the computational domain and the index j refers to those immersed boundaries whose nodes are already aligned with the Cartesian background grid. Eqn. (21) is solved component wise for d_x and d_y, and the vertices of the final mesh are updated only after convergence,

$$\mathbf{x}_{\text{new}} = \mathbf{x}_{\text{old}} + \mathbf{d}. \tag{22}$$



(a) full domain

(b) magnified view near the cylinder surface

Fig. 2: Finite element mesh for natural convection around a heated cylinder in a cold square cavity.

Once the vertices are updated through Eqn. (22), each background cell (i_1, i_2, i_3, i_4) of $\mathcal{G}$ is reconstructed from the multiplicities ν stored at its four corners. Cells with $\nu = 1$ at every corner keep the original quadrilateral topology. Cells with a pair of split corners on the same edge collapse into a triangle. Cells that carry a single split corner opposite a fully interior corner produce a pentagon, which is then split into one triangle and one quadrilateral along the diagonal that emanates from the split vertex. The full computational domain is shown in Fig. 2a and Fig. 2b shows a magnified view near the cylinder, where the three cell topologies produced by the algorithm (triangular, quadrilateral, and the pentagon split into a triangle plus a quadrilateral) are clearly visible.

3.2 Numerical solution procedure

The dimensionless governing equations (6)-(9), with the Dirichlet velocity and temperature conditions stated in Section 2.2, are advanced on the body conforming mesh of Section 3.1 using a pressure based finite element method. The spatial operators are discretized by a classical Galerkin scheme with equal order bilinear interpolation for all primitive variables (u, v, p, θ), and the time evolution is carried out by an explicit fractional step (projection) algorithm [13, 44] with a second-order Adams-Bashforth treatment of the convection-diffusion operator. The pressure Poisson equation that arises from the incompressibility constraint is solved at every time step by a warm started Conjugate Gradient iteration, and the surface integrated Nusselt numbers are extracted in a post-processing step from the dimensionless temperature gradient. The four building blocks of the algorithm, namely the spatial discretizations, the time integration, the pressure solver, and the Nusselt number evaluation, are described in Sections 3.2.1-3.2.5 below.

3.2.1 Galerkin finite element spatial discretizations

The computational domain is discretized into N_e elements by the grid generation procedure of Section 3.1. The dominant cell type is the four-node bilinear quadrilateral (Q_4). On a generic Q_4 element Ω^e the primary unknowns are interpolated from nodal values using the standard bilinear Lagrangian shape functions defined on the reference square $(\xi, \eta) \in [-1, 1]^2$ [22, 50],

$$N_1 = \tfrac{1}{4}(1-\xi)(1-\eta), \quad N_2 = \tfrac{1}{4}(1+\xi)(1-\eta), \quad N_3 = \tfrac{1}{4}(1+\xi)(1+\eta), \quad N_4 = \tfrac{1}{4}(1-\xi)(1+\eta). \tag{23}$$

Each primary variable $\phi \in \{u, v, p, \theta\}$ is approximated element wise as $\phi^e(x, y) = \sum_{k=1}^{4} N_k(\xi, \eta)\, \phi_k$, so the formulation is an equal order Q_4/Q_4 element [6, 16]. The mapping from the reference element to the physical element uses the same shape functions (iso-parametric mapping), and the Jacobian $\mathbf{J} = \partial(x, y)/\partial(\xi, \eta)$ links the natural and physical derivatives, $\nabla_{\mathbf{x}} N_k = \mathbf{J}^{-1} \nabla_{\xi} N_k$.

Multiplying Eqns. (7)-(9) by a test function N_i drawn from the same space, integrating over Ω^e, and applying the divergence theorem to the viscous and thermal diffusion terms gives the standard Galerkin weak form [16]. Collecting the coefficients, the element level interpolation generates four matrices that depend only on the geometry and are therefore *computed once* during pre-processing and stored,

$$\mathbf{K}^e_{ij} = \int_{\Omega^e} \left(\frac{\partial N_i}{\partial x} \frac{\partial N_j}{\partial x} + \frac{\partial N_i}{\partial y} \frac{\partial N_j}{\partial y} \right) \mathrm{d}\Omega, \tag{24}$$

$$C^{x,e}_{ij} = \int_{\Omega^e} N_i \frac{\partial N_j}{\partial x}\, \mathrm{d}\Omega, \qquad C^{y,e}_{ij} = \int_{\Omega^e} N_i \frac{\partial N_j}{\partial y}\, \mathrm{d}\Omega, \tag{25}$$

$$M^e_{ij} = \int_{\Omega^e} N_i N_j\, \mathrm{d}\Omega, \qquad m^e_i = \int_{\Omega^e} N_i\, \mathrm{d}\Omega. \tag{26}$$

The matrix $\mathbf{K}^e$ is the diffusion (stiffness) matrix common to the viscous and thermal operators. The matrices $C^{x,e}$ and $C^{y,e}$ are the advection matrices that are contracted with the element centroid velocity. M^e is the consistent mass matrix and m^e_i is its row sum. The row sum provides the diagonal *lumped* mass that is used in the explicit time advance. This is a standard device that conserves total mass without the cost of a linear solve at each step [22, 50].

All element integrals in Eqns. (24)-(26) are evaluated by a 2×2 Gauss-Legendre quadrature on the reference element, with integration points at $\xi, \eta = \pm 1/\sqrt{3}$ and unit weights. This rule integrates the bilinear polynomials that appear in $\mathbf{K}^e$ and M^e exactly on parallelogram elements and is sufficiently accurate for the mildly distorted quadrilaterals generated by the grid algorithm [50]. For the small set of triangular cells at the cylinder interface, the standard closed-form expressions for linear triangular (P_1) elements are used in place of the quadrature rule.

The mesh is Eulerian and stays fixed throughout the run. The element matrices (24)-(26) are therefore built once at the start, kept in a compact element-by-element (EBE) storage [9, 23], and reused at every time step.

3.2.2 Fractional-step time integration

The pressure-velocity coupling in Eqns. (6)-(8) is handled by the fractional-step (projection) method introduced by Chorin [13] and Temam [44] and analyzed for finite elements by Guermond et al. [19] and earlier implemented in [28, 29]. The advance from t_n to $t_{n+1} = t_n + \Delta t$ is split into three sub-steps: a *predictor* that computes an auxiliary, generally non-solenoidal, velocity by ignoring the pressure gradient; a Poisson equation for the pressure that encodes the incompressibility constraint; and a *corrector* that projects the auxiliary field onto the space of divergence-free velocities.

Predictor

A forward Euler step of Eqns. (7)-(9), without the pressure gradient, leads to an element contribution to the nodal residual of the form

$$\mathbf{f}_u^{e,n} = \Delta t \sum_{j=1}^{4} \Big[-Pr\, \mathbf{K}_{ij}^e - \big(u_c^{e,n}\, C_{ij}^{x,e} + v_c^{e,n}\, C_{ij}^{y,e} \big) \Big] u_j^n, \tag{27}$$

$$\mathbf{f}_v^{e,n} = \Delta t \sum_{j=1}^{4} \Big[-Pr\, \mathbf{K}_{ij}^e - \big(u_c^{e,n}\, C_{ij}^{x,e} + v_c^{e,n}\, C_{ij}^{y,e} \big) \Big] v_j^n + Ra\, Pr\, \Delta t\, \bar{\theta}^{e,n}\, m_i^e, \tag{28}$$

$$\mathbf{f}_\theta^{e,n} = \Delta t \sum_{j=1}^{4} \Big[-\mathbf{K}_{ij}^e - \big(u_c^{e,n}\, C_{ij}^{x,e} + v_c^{e,n}\, C_{ij}^{y,e} \big) \Big] \theta_j^n, \tag{29}$$

where the convective velocity $(u_c^{e,n}, v_c^{e,n})$ is separately evaluated and calculated at element centroid velocity at the previous time step and $\bar{\theta}^{e,n} = \frac{1}{n_{en}} \sum_{k=1}^{n_{en}} \theta_k^n$ ($n_{en} = 3$ for triangle and $n_{en} = 4$ for quadrilateral) is the element-averaged temperature that enters the Boussinesq buoyancy source. The last term of Eqn. (28) is the discrete counterpart of the $Ra\, Pr\, \theta$ source in Eqn. (8).

Adams-Bashforth extrapolation

Equations (27)-(29) form a first-order Euler estimate. To raise the time accuracy to second order, each right-hand side $\mathbf{f}^n$ is replaced by its two-step Adams-Bashforth extrapolation [3, 8],

$$\mathbf{f}^{n+\frac{1}{2}} = \begin{cases} \mathbf{f}^n, & n = 1 \text{ (Euler initialization)}, \\ \frac{3}{2}\mathbf{f}^n - \frac{1}{2}\mathbf{f}^{n-1}, & n > 1, \end{cases} \tag{30}$$

where $\mathbf{f}^{n-1}$ is stored from the previous step. The element contributions are then scattered to the global nodal arrays and divided by the lumped diagonal mass $d_i =$

$\sum_{e\ni i} m_i^e$ (the row-sum mass-lumping of Eqn. (26)), which gives the explicit update for the intermediate velocity $\mathbf{u}^*$ and the final temperature θ^{n+1} at every *interior* node i,

$$u_i^* = u_i^n + d_i^{-1}\sum_{e\ni i} f_{u,i}^{e,n+1/2}, \quad v_i^* = v_i^n + d_i^{-1}\sum_{e\ni i} f_{v,i}^{e,n+1/2}, \quad \theta_i^{n+1} = \theta_i^n + d_i^{-1}\sum_{e\ni i} f_{\theta,i}^{e,n+1/2}. \tag{31}$$

Nodes that lie on the cavity walls or on the cylinder surface are excluded from Eqn. (31); their velocity and temperature are held at the prescribed Dirichlet values stated in Section 2.1, which in finite element terms is the strong imposition of essential boundary conditions [22].

Pressure Poisson equation

Taking the divergence of the formally corrected momentum equation $\mathbf{u}^{n+1} = \mathbf{u}^* - \Delta t\,\nabla p^{n+1}$ and imposing the continuity constraint $\nabla\cdot\mathbf{u}^{n+1} = 0$ gives the pressure Poisson equation $\nabla^2 p^{n+1} = (1/\Delta t)\,\nabla\cdot\mathbf{u}^*$ [19]. In the discrete setting, after absorbing the time step into the pressure variable, the element level divergence of the intermediate velocity is evaluated edge-wise with the midpoint rule,

$$D^e = \sum_{\text{edges}} \Big[\tfrac{1}{2}(u_{m_1}^* + u_{m_2}^*)\,\Delta y_{\text{edge}} - \tfrac{1}{2}(v_{m_1}^* + v_{m_2}^*)\,\Delta x_{\text{edge}}\Big], \tag{32}$$

where (m_1, m_2) are the two endpoint nodes of each element edge and $(\Delta x_{\text{edge}}, \Delta y_{\text{edge}})$ are its coordinate increments. The element divergences D^e are then scattered to the nodes through the lumped-mass weights to produce the source vector

$$b_i = d_i^{-1}\sum_{e\ni i} m_i^e\, D^e, \tag{33}$$

and the discrete pressure Poisson system for an element reads

$$\mathbf{A}_{ij}^e\; P_j^e = b_i^e, \tag{34}$$

where $\mathbf{A_{ij}^e}$ is the element matrix for the equation for pressure and thus forms a symmetric positive semi-definite system.

3.2.3 Cell centre and nodal velocity correction

Once p^{n+1} is available, the pressure gradient is recovered at the element centroid $(\xi, \eta) = (0, 0)$,

$$\left.\frac{\partial p}{\partial x}\right|_e = \sum_{k=1}^{n_{en}} \frac{\partial N_k}{\partial x}\Big|_{(0,0)} p_k^{n+1}, \qquad \left.\frac{\partial p}{\partial y}\right|_e = \sum_{k=1}^{n_{en}} \frac{\partial N_k}{\partial y}\Big|_{(0,0)} p_k^{n+1}. \tag{35}$$

The element centroid velocities that enter the next-step advection operator in Eqns. (27)-(29) are corrected as

$$u_c^{e,n+1} = \tfrac{1}{4}\sum_{k=1}^{4} u_k^* - \left.\frac{\partial p}{\partial x}\right|_e, \qquad v_c^{e,n+1} = \tfrac{1}{4}\sum_{k=1}^{4} v_k^* - \left.\frac{\partial p}{\partial y}\right|_e, \tag{36}$$

The cell centre velocity components are corrected using the gradient of the evaluated pressure without any interpolations. The nodal velocity components are corrected by projecting the element centroid pressure gradient back to the nodes through the lumped mass,

$$u_i^{n+1} = u_i^* - d_i^{-1} \sum_{e \ni i} m_i^e \left.\frac{\partial p}{\partial x}\right|_e , \qquad v_i^{n+1} = v_i^* - d_i^{-1} \sum_{e \ni i} m_i^e \left.\frac{\partial p}{\partial y}\right|_e . \tag{37}$$

As in the predictor, Eqn. (37) is applied only at interior nodes, and the no-slip condition on the walls and on the cylinder is preserved exactly. The loop then returns to Eqn. (27) for the next time step. The time step $\Delta t = 10^{-7}$ used throughout this work was selected to satisfy both the convective (CFL < 1) and the diffusive ($\Delta t < h^2/(4\,Pr)$) stability limits of the explicit scheme [18] with a comfortable safety margin.

3.2.4 Solution of the pressure Poisson equation

The symmetric positive semi-definite system Eqn. (34) is solved at every time step by the Conjugate Gradient (CG) method, which is the canonical iterative solver for such systems and shows finite step termination in exact arithmetic [4, 40]. Three practical features of the present implementation are worth highlighting.

The first feature is the Element-By-Element(EbE) matrix-free product. The global matrix $\mathbf{A}$ in Eqn. (34) is *never* assembled or stored. Each CG iteration only needs the matrix-vector product $\mathbf{q} = \mathbf{A}\mathbf{d}$, which is evaluated element-by-element from the pre-computed stiffness matrices $\mathbf{A}^e$ as

$$(\mathbf{A}\mathbf{d})_i = \sum_{e \ni i} \sum_{j=1}^{4} \mathbf{A}_{ij}^e \, d_{\,\mathrm{node}(j,e)} . \tag{38}$$

This EbE strategy, originally introduced by Hughes et al. [23] for explicit dynamics and recently reported for stream function in [28], is particularly effective on unstructured meshes with mixed element types, since it avoids the bookkeeping of a sparse matrix.

The second feature is the warm-started initial guess. The pressure field is continuous in time and changes only slightly between consecutive steps, in particular at the small Δt used here. The CG iteration at step $n+1$ is therefore initialized with the solution from step n, $\mathbf{p}_{n+1}^{(0)} = \mathbf{p}^n$. This warm start usually brings convergence in only a few iterations per time step, well below the maximum of ten iterations imposed as a safeguard.

The third feature is shared memory parallelism. All inner loops of the CG algorithm, namely the EbE matrix-vector products (Eqn. (38)), the scatter-add assemblies, the vector updates, and the reduction dot products, are parallelized with OpenMP [34] through static work-sharing of element and node-index ranges. Scatter add operations, which accumulate element contributions into shared nodal arrays, are protected by `$OMP ATOMIC` directives to avoid race conditions, while dot products use the `REDUCTION(+:)` clause for lock-free global summation.

The convergence criterion $\|\mathbf{r}\|_2^2 < \varepsilon_{\mathrm{CG}}$ with $\varepsilon_{\mathrm{CG}} = 10^{-17}$ drives the residual down to the level of double precision round off, so that the velocity projection in Eqn. (37) enforces incompressibility to machine accuracy.

3.2.5 Nusselt number evaluation

The integral heat transfer quantities reported in this work are the surface averaged Nusselt number on the heated cylinder, $\overline{Nu}_{\mathrm{cyl}}$, and its counterpart integrated over the four cold walls of the cavity, $\overline{Nu}_{\mathrm{walls}}$. The bilinear Q_4 interpolation in Eqn. (23) gives a temperature field that is C^0-continuous but whose gradient is piecewise constant (one value per element) and therefore discontinuous across element edges. A *recovery* step is therefore used to obtain a second order accurate nodal gradient field before the boundary integrals are evaluated. The recovery is described first, followed by the Nusselt number formulas for the cylinder and the walls.

Element-centroid temperature gradient

The gradient of the temperature field inside each element is evaluated at the element centroid $(\xi, \eta) = (0, 0)$ in exactly the same way as the pressure gradient in Eqn. (35), with θ in place of p,

$$\left(\tfrac{\partial\theta}{\partial x}\big|_e,\ \tfrac{\partial\theta}{\partial y}\big|_e\right) = \sum_{k=1}^{4}\left(\tfrac{\partial N_k}{\partial x},\ \tfrac{\partial N_k}{\partial y}\right)_{(0,0)}\theta_k. \tag{39}$$

Nodal gradient by patch averaging

Let $\mathcal{E}_i = \{e : i \in \Omega^e\}$ denote the patch of $|\mathcal{E}_i|$ elements that share node i. The nodal temperature gradient is obtained by simple arithmetic averaging over the patch,

$$\tfrac{\partial\theta}{\partial x}\big|_i = \frac{1}{|\mathcal{E}_i|}\sum_{e\in\mathcal{E}_i}\tfrac{\partial\theta}{\partial x}\big|_e, \qquad \tfrac{\partial\theta}{\partial y}\big|_i = \frac{1}{|\mathcal{E}_i|}\sum_{e\in\mathcal{E}_i}\tfrac{\partial\theta}{\partial y}\big|_e. \tag{40}$$

On uniform patches this procedure is equivalent to the super-convergent patch recovery (SPR) technique of Zienkiewicz and Zhu [49] and is known to deliver nodal gradients that are accurate one full order beyond the underlying finite element solution.

Nusselt number

The local Nusselt number along any boundary surface $\mathcal{S}$ (the cylinder perimeter or any of the four cavity walls) is defined as

$$Nu(s) = \left|\frac{\partial\theta}{\partial n}\right|, \tag{41}$$

where s is the arc length measured along $\mathcal{S}$ and $\hat{\mathbf{n}}$ is the outward unit normal. For two consecutive boundary nodes $(\mathbf{x}_b^{(l)}, \mathbf{x}_b^{(l+1)})$ separated by a segment of length $\delta\ell_l = \|\mathbf{x}_b^{(l+1)} - \mathbf{x}_b^{(l)}\|$, the outward normal direction is $\hat{\mathbf{n}}_l = (\Delta y_l, -\Delta x_l)/\delta\ell_l$, where Δx_l and Δy_l are the segment components. Using the segment-averaged nodal gradients $\bar{g}_{x,l} = \frac{1}{2}(\partial\theta/\partial x|_l + \partial\theta/\partial x|_{l+1})$ and the analogous $\bar{g}_{y,l}$, the normal gradient along the segment is

$$\left.\frac{\partial\theta}{\partial n}\right|_l = \frac{\left|\bar{g}_{x,l}\,\Delta y_l - \bar{g}_{y,l}\,\Delta x_l\right|}{\delta\ell_l}. \tag{42}$$

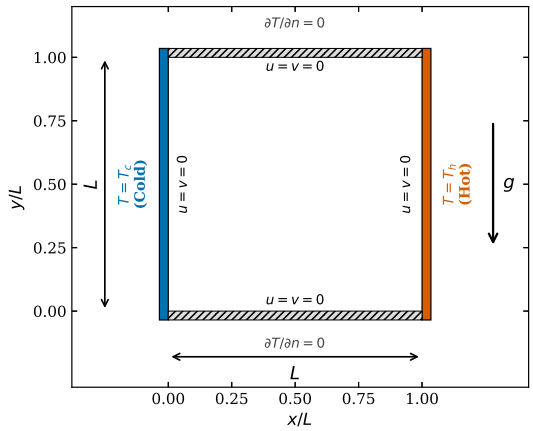


Fig. 3: Schematic of the De Vahl Davis benchmark: differentially heated square cavity with insulated top and bottom walls.

The surface-averaged Nusselt number over any boundary $\mathcal{S}$ composed of N_b segments with total perimeter $\mathcal{L}_\mathcal{S}$ is then

$$\overline{Nu}_\mathcal{S} = \frac{1}{\mathcal{L}_\mathcal{S}} \sum_{l=1}^{N_b} \left.\frac{\partial \theta}{\partial n}\right|_l \delta\ell_l. \tag{43}$$

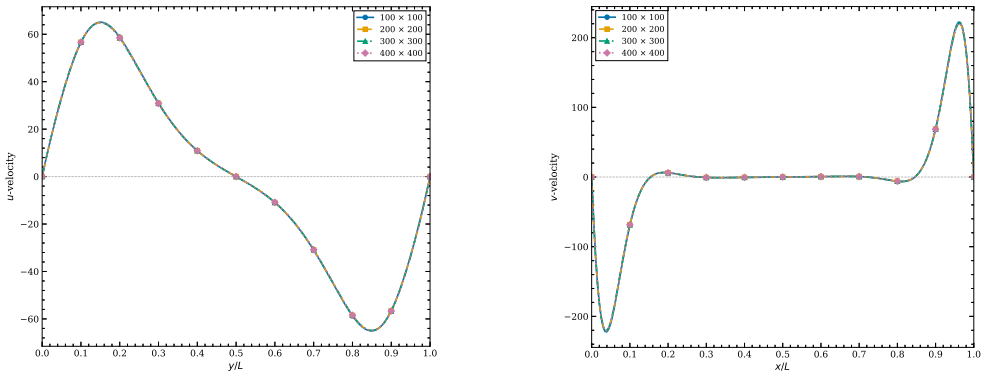
When $\mathcal{S}$ is the heated cylinder, $\mathcal{L}_\mathcal{S} = \pi D$ with $D = 2R = 0.4$, and Eqn. (43) gives $\overline{Nu}_{\text{cyl}}$. When $\mathcal{S}$ is any individual cavity wall of length L, $\mathcal{L}_\mathcal{S} = L$ and the same expression gives the wall-averaged Nusselt number $\overline{Nu}_{\text{wall}}$. For the four cold walls taken together, the total perimeter is $\mathcal{L}_\mathcal{S} = 4L$ and the summation runs over all wall segments, yielding the enclosure-averaged Nusselt number $\overline{Nu}_{\text{walls}}$.

4 Validation of the Code

The solver is validated against the classical differentially heated square cavity benchmark of De Vahl Davis [14], refined subsequently by Hortmann et al. [21] and Le Quéré [30]. This benchmark is the standard test case for buoyancy driven flow in closed geometries and carries a large body of accurate reference data, making it well suited to confirm that the spatial discretizations, fractional-step time integrator, and the implementation of Conjugate Gradient pressure solver.

The geometry is a square cavity of side L filled with air ($Pr = 0.71$), as shown in Fig. 3. The right wall is held at the hot temperature T_h and the left wall at the cold temperature $T_c < T_h$; the top and bottom walls are thermally insulated ($\partial T/\partial n = 0$). The validation is performed at $Ra = 10^6$, which lies well within the laminar steady regime and produces boundary layers sharp enough to be a demanding test of the spatial discretizations.

Four uniform Cartesian grids 100×100, 200×200, 300×300, and 400×400 cells are tested using the horizontal velocity u along the vertical midline ($x/L = 0.5$) and



(a) Horizontal velocity $u(y)$ at $x/L = 0.5$.

(b) Vertical velocity $v(x)$ at $y/L = 0.5$.

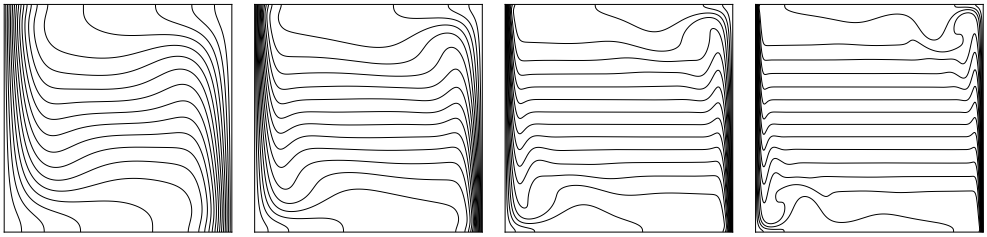
Fig. 4: Grid independence study for the De Vahl Davis benchmark at $Ra = 10^6$, $Pr = 0.71$.

the vertical velocity v along the horizontal midline ($y/L = 0.5$) as monitors. These profiles are standard grid sensitivity indicators for this benchmark [14, 30] since they capture both the boundary layer structure along the active walls and the strength of the central recirculating core.

As seen in Fig. 4, the four curves are visually indistinguishable in both panels, with no shift in peak velocity locations or magnitudes between successive refinements. This confirms that the solution is grid independent already on the 100×100 mesh.

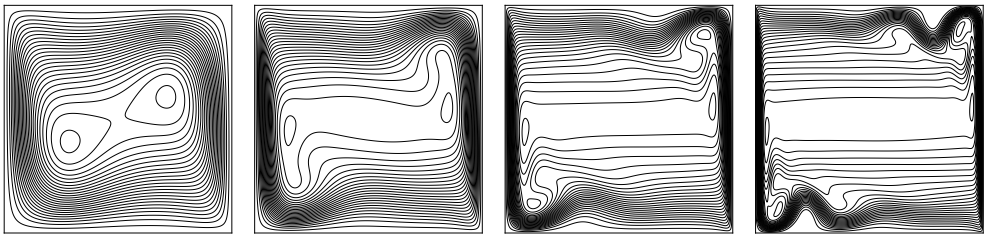
The present solution computed on the 300×300 grid is now compared with the high accuracy reference data of De Vahl Davis [14] and Le Quéré [30], as well as with several other published numerical studies [1, 12, 17, 25, 48]. The comparison covers four Rayleigh numbers ($Ra = 10^5$, 10^6, 10^7, and 10^8). The isotherms for all four Rayleigh numbers are shown in Fig. 5 and the corresponding streamlines in Fig. 6. At $Ra = 10^5$, the isotherms are nearly vertical, indicating that heat transfer is still largely conduction dominated. As Ra increases to 10^6 and beyond, the isotherms progressively tilt toward horizontal stratification, which is the signature of strong convective transport. By $Ra = 10^8$, the temperature gradients are concentrated into thin layers adjacent to the hot and cold walls, while the core of the cavity is nearly isothermal. The streamlines show a complementary evolution: the single recirculating cell at $Ra = 10^5$ gradually tightens and the contour lines crowd near the active walls at higher Ra, reflecting the intensification of the boundary layer driven circulation. Both the isotherm patterns and the streamline topology are in close visual agreement with the published contours [14, 30].

Table 1 summarizes the average Nusselt number $\overline{Nu}$, the maximum horizontal velocity $u_{\max}$ along the vertical mid-line, the maximum vertical velocity $v_{\max}$ along the horizontal mid-line, and the peak stream-function value ψ_{mid} for each Rayleigh number. These four quantities together probe the thermal performance of the cavity, the strength of the boundary layer jets, and the overall intensity of the recirculation.



(a) $Ra = 10^5$ (b) $Ra = 10^6$ (c) $Ra = 10^7$ (d) $Ra = 10^8$

Fig. 5: Isotherms of natural convection inside a differentially heated square cavity for $10^5 \leq Ra \leq 10^8$, $Pr = 0.71$.



(a) $Ra = 10^5$ (b) $Ra = 10^6$ (c) $Ra = 10^7$ (d) $Ra = 10^8$

Fig. 6: Streamlines of natural convection inside a differentially heated square cavity for $10^5 \leq Ra \leq 10^8$, $Pr = 0.71$.

5 Results and discussion

5.1 Grid convergence study

The discretizations uncertainty is quantified using the standardized Grid Convergence Index (GCI) methodology of Celik [11], which combines the Richardson extrapolation framework of [37] with the GCI formulation of Roache [38]. The procedure yields a safety-factor weighted percentage uncertainty on any integral quantity of interest. The surface-averaged cylinder Nusselt number $\overline{Nu}_{\text{cyl}}$ is chosen as the monitor variable since it is the principal heat transfer output of the simulation. Four uniform Cartesian grids of 100×100, 200×200, 300×300, and 400×400 cells are used, with a representative mesh spacing $h = L/N_x$ ranging from 0.01 down to 0.0025. All grid metrics and the derived GCI quantities are given in Table 2.

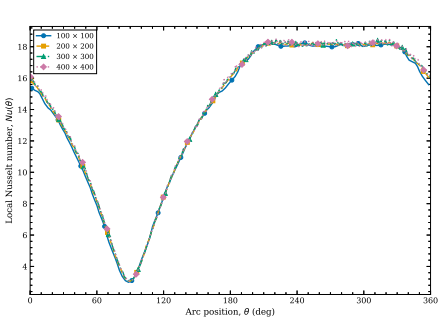
The GCI analysis is restricted to the three finest grids, as recommended by Celik [11]; the coarsest grid is retained only for qualitative context. The successive refinement ratios are $r_{21} = 1.333$ and $r_{32} = 1.500$, both above the recommended minimum of 1.3. Iterative solution of the nonlinear order equation gives an apparent order of accuracy $p = 0.7734$. This value is lower than the formal second order of the bilinear Galerkin discretization because of three combined effects: the row-sum lumped

Table 1: Comparison of present results with published results for the differentially heated square cavity

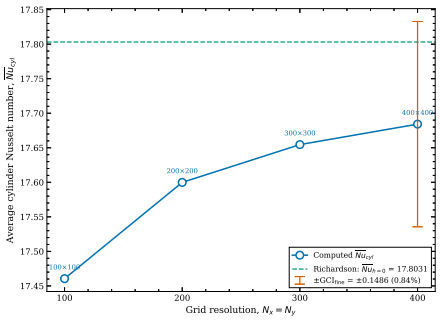
Reference	$\overline{Nu}$	$u_{\max}$	$v_{\max}$	ψ_{mid}
$Ra = 10^5$				
De Vahl Davis [14]	4.519	34.73	68.59	9.111
Chenoweth & Paolucci [12]	4.520	34.77	68.63	-
Kalita et al. [25]	4.522	34.825	68.61	9.123
Yu & Tian [48]	4.5526	34.6856	68.5748	9.1093
Present work	**4.5214**	**34.8264**	**68.6516**	**9.1163**
$Ra = 10^6$				
De Vahl Davis [14]	8.817	64.63	219.36	16.32
Chenoweth & Paolucci [12]	8.874	63.76	218.8	-
Le Quéré [30]	8.8252	64.8344	220.56	16.3864
Kalita et al. [25]	8.763	65.332	221.658	16.42
Yu & Tian [48]	8.8235	64.7187	220.377	16.3657
Dutta et al. [17]	8.7721	64.4527	217.442	16.3409
Present work	**8.8246**	**64.9342**	**220.7725**	**16.3924**
$Ra = 10^7$				
Chenoweth & Paolucci [12]	16.82	146	699	-
Le Quéré [30]	16.523	148.59	699.17	29.361
Kalita et al. [25]	16.075	155.82	696.238	29.382
Yu & Tian [48]	16.489	147.6246	696.857	29.3126
Xu et al. [1]	16.52229	148.57189	699.33994	29.36267
Dutta et al. [17]	16.2525	144.406	672.739	29.06041
Present work	**16.5577**	**149.0287**	**700.6196**	**29.3824**
$Ra = 10^8$				
Le Quéré [30]	30.255	321.878	2222.39	52.3223
Xu et al. [1]	30.2265	320.9883	2223.4660	52.3265
Dutta et al. [17]	29.9898	304.344	2184.62	50.7929
Present work	**30.5421**	**343.8847**	**2230.6075**	**52.9973**

mass matrix used in the explicit time advance, which is known to reduce the formal spatial order in many norms [22]; the first-order pressure splitting introduced by the Chorin-Temam fractional-step method [13, 19, 44]; and the piecewise-linear approximation of the curved cylinder boundary on the body-fitted Cartesian background mesh. The observed value lies within the range commonly reported for lumped-mass projection finite element schemes. The signs of the successive solution differences ε_{21} and ε_{32} are both negative, which confirms monotonic convergence and validates the use of Richardson extrapolation [38]. The extrapolated continuum value in the $h \to 0$ limit is $\overline{Nu}_{h=0} = 17.8031$.

The resulting fine-grid uncertainty $\mathrm{GCI}_{\mathrm{fine}} = 0.84\,\%$ falls well below the widely adopted $1\,\%$ threshold and confirms grid independence. The asymptotic ratio $\mathcal{R}_{\mathrm{asymp}} = 1.0017 \approx 1$ shows that the solution sits firmly inside the asymptotic range, so the observed order is fully consistent with the formal order of the underlying discretizations [11]. As an additional physical check, the global energy imbalance between



(a) Circumferential distribution of the local Nusselt number $Nu(\theta)$ for all four grids.



(b) Average cylinder Nusselt number versus grid resolution with Richardson extrapolation and GCI uncertainty.

Fig. 7: Grid convergence for natural convection at $Ra = 10^6$, $Pr = 0.71$.

Table 2: Consolidated grid convergence and GCI analysis for natural convection at $Ra = 10^6$, $Pr = 0.71$ for four different grids (100×100 to 400×400) with safety factor $F_s = 1.25$.

(a) Per-grid data

Grid label	$N_x \times N_y$	h	$\overline{Nu}_{\mathrm{cyl}}$	$\delta\overline{Nu}$ (%)	$\overline{Nu}_{\mathrm{walls}}$	E_{imb} (%)
Coarse	100×100	0.01000	17.4605	—	17.7925	1.866
Medium-low	200×200	0.00500	17.5999	0.792	17.7778	1.001
Medium-high	300×300	0.00333	17.6546	0.310	17.7756	0.681
Fine	400×400	0.00250	17.6842	0.168	17.7751	0.512

(b) GCI analysis (three finest grids)

Parameter	Value
Refinement ratio r_{21}	1.3333
Refinement ratio r_{32}	1.5000
Apparent order p	0.7734
Richardson extrapolation $\overline{Nu}_{h=0}$	17.8031
Approx. relative error $e_{a,21}$	0.168 %
Approx. relative error $e_{a,32}$	0.310 %
$\mathrm{GCI}_{\mathrm{fine}}$ ($400 \times 400 \leftarrow 300 \times 300$)	0.84 %
$\mathrm{GCI}_{\mathrm{medium}}$ ($300 \times 300 \leftarrow 200 \times 200$)	1.05 %
Asymptotic ratio $\mathcal{R}_{\mathrm{asymp}}$	$1.0017 \approx 1$

the heat released by the cylinder and the heat absorbed by the cavity walls falls monotonically from 1.87 % on the coarsest grid to 0.51 % on the 400×400 grid (Table 2), which confirms consistency across the entire grid sequence.

The circumferential distribution of the local Nusselt number $Nu(\theta)$ along the cylinder perimeter is shown in Fig. 7a for all four grids. The three finest grids overlap visually over most of the arc, and only the coarsest 100×100 result deviates

Table 3: Flow statistics for steady natural convection around a heated cylinder placed inside a square cavity ($Pr = 0.71$).

Quantity	$Ra = 10^4$	$Ra = 10^5$	$Ra = 10^6$	$Ra = 5 \times 10^6$
$\psi_{\max}$	1.005	8.350	24.211	34.614
$\psi_{\min}$	-1.005	-8.350	-24.211	-35.872
$\lvert u\rvert_{\max}$	5.973	51.345	232.172	579.675
$\lvert v\rvert_{\max}$	8.152	70.602	254.610	624.089
$\lvert \mathbf{V}\rvert_{\max}$	8.978	76.380	267.155	624.181
$\lvert \omega\rvert_{\max}$	463.4	4551.6	24062.4	62865.4
$\overline{Nu}_{\mathrm{cyl}}$	6.401	9.745	17.655	25.147
$\overline{Nu}_{\mathrm{encl}}$	6.444	9.813	17.776	25.298

noticeably near the separation point at $\theta \approx 60^\circ$ and inside the upper plume region $180^\circ \lesssim \theta \lesssim 240^\circ$. Fig. 7b shows the monotonic refinement history of $\overline{Nu}_{\mathrm{cyl}}$ together with the Richardson extrapolated limit and the $\pm\mathrm{GCI}_{\mathrm{fine}}$ uncertainty band on the 400×400 result. The extrapolated value lies inside this band, which is further evidence that the simulation is in the asymptotic regime. The result on the finest grid is

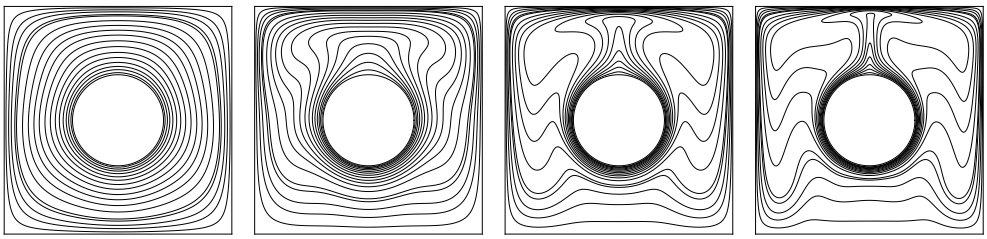
$$\overline{Nu}_{\mathrm{cyl}} = 17.6842 \pm 0.1486 \quad \left(\mathrm{GCI}_{\mathrm{fine}} = 0.84\,\%\right). \tag{44}$$

The accuracy gain of the 400×400 grid over the 300×300 grid is only $\delta\overline{Nu} = 0.168\,\%$, while its computational cost is substantially higher. The 300×300 grid satisfies the grid independence criterion with $\mathrm{GCI} = 1.05\,\%$ and $E_{\mathrm{imb}} = 0.68\,\%$, and is therefore adopted for all subsequent parametric simulations reported in this work.

5.2 Steady-State Results ($Ra = 10^4$ to 5×10^6)

The steady state behaviour of natural convection around a heated cylinder placed concentrically inside a cold square cavity is analyzed for Rayleigh numbers from 10^4 up to 5×10^6, keeping the Prandtl number fixed at $Pr = 0.71$ (air). The buoyancy driven flow that develops in the annular gap between the cylinder and the cavity walls is examined through isotherms and streamlines, and the corresponding flow statistics are summarized in Table 3. The table also reports the surface averaged Nusselt number on the cylinder, $\overline{Nu}_{\mathrm{cyl}}$, and the area averaged value on the four cavity walls, $\overline{Nu}_{\mathrm{encl}}$. By global energy balance these two quantities should be equal, and the small residual difference (less than 0.7% at every Rayleigh number) is the energy balance error of the present simulation.

As the Rayleigh number is raised by nearly three orders of magnitude (from 10^4 to 5×10^6), the maximum stream function value grows from about 1.0 to nearly 36, and the peak velocity magnitude rises from about 9 to roughly 624. The maximum vorticity climbs by more than two orders of magnitude, from 4.6×10^2 at $Ra = 10^4$ to 6.3×10^4 at $Ra = 5 \times 10^6$, which means that the velocity gradients in the boundary



(a) $Ra = 10^4$ (b) $Ra = 10^5$ (c) $Ra = 10^6$ (d) $Ra = 5 \times 10^6$

Fig. 8: Isotherms of natural convection around a heated cylinder placed inside a square cavity for $10^4 \leq Ra \leq 5 \times 10^6$, $Pr = 0.71$.

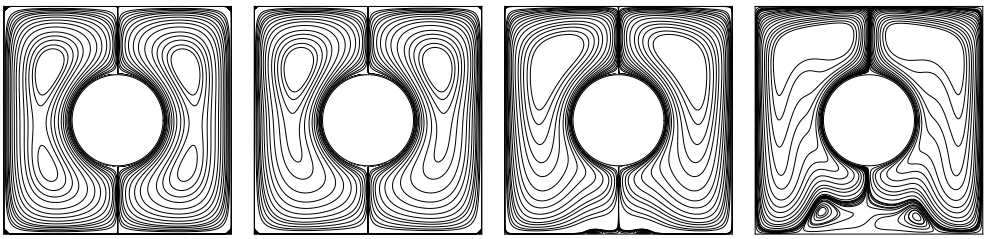
layers near the heated cylinder and the cold cavity walls become very steep at the high Rayleigh number end of the range. A clear left right split of the stream function also appears at $Ra = 5 \times 10^6$: the magnitude of the negative core $|\psi_{\min}| = 35.87$ exceeds the magnitude of the positive core $\psi_{\max} = 34.61$ by about 3.6%. The variation in the two values is the first physical signature of the broken symmetry mode that grows further at higher Rayleigh numbers and is fully developed in the unsteady regime described in Section 5.4. The amplitude of the deviation is still small enough that the spatial contour plots look mirror symmetric to the eye. This case is therefore reported in steady state results with the understanding that at $Ra = 5 \times 10^6$ the steady symmetric solution has just begun to lose a small fraction of its stability.

5.2.1 Isotherms

Figure 8 presents the isotherm contours for the four Rayleigh numbers. These contours show how the temperature is distributed in the annular gap between the hot cylinder and the cold square walls. The transition from conduction dominated transport to convection dominated transport is clearly visible as the Rayleigh number is increased.

At $Ra = 10^4$ (Figure 8a), the isotherms appear as nearly concentric circles centered on the cylinder. The temperature drops smoothly and almost uniformly in all directions from the hot cylinder surface towards the cold cavity walls. This pattern closely resembles a pure conduction solution which tells us that buoyancy forces are not yet strong enough to significantly distort the thermal field. The contours are almost symmetric about both the horizontal and vertical centre lines of the cavity. A very faint upward shift of the isotherms can be seen on close inspection, indicating that a weak convective motion has just started to develop.

When the Rayleigh number is increased to $Ra = 10^5$ (Figure 8b), the isotherms undergo noticeable distortion. The contours in the upper half of the cavity are pushed upwards and become compressed against the top wall, marking the beginning of a thermal plume above the cylinder. This happens because the heated fluid, being lighter, rises from the cylinder surface and carries thermal energy upwards. At the same time, the isotherms in the lower portion of the cavity become more widely spaced, indicating a slower rate of temperature change in that region. The thermal field is no longer symmetric about the horizontal mid plane, although the left right symmetry about



(a) $Ra = 10^4$ (b) $Ra = 10^5$ (c) $Ra = 10^6$ (d) $Ra = 5 \times 10^6$

Fig. 9: Streamlines of natural convection around a heated cylinder placed inside a square cavity for $10^4 \leq Ra \leq 5 \times 10^6$, $Pr = 0.71$.

the vertical mid plane is still maintained. The compression of isotherms near the top wall implies a large local temperature gradient, which leads to enhanced heat transfer at the upper part of the enclosure. This shift from a conduction dominated regime to one in which convection begins to play a noticeable role is a classic feature of natural convection in enclosures described by Moukalled and Acharya [32].

At $Ra = 10^6$ (Figure 8c), the convective effects become much stronger and the isotherm pattern changes significantly. A well defined thermal plume is now clearly visible above the cylinder where the hot fluid rises in a narrow concentrated column before spreading sideways as it hits the top wall. The isotherms in this plume region are tightly packed, showing a steep temperature gradient. Below the cylinder the isotherms are widely spaced and nearly horizontal, indicating thermal stratification because the fluid in the lower part of the cavity is relatively stagnant and the temperature there varies slowly. The isotherms on the sides of the cylinder show a characteristic S-shaped or wavy distortion, which is caused by the recirculating flow that sweeps hot fluid upwards along the cylinder surface and brings cold fluid downwards along the cavity side walls. The thermal boundary layer on the cylinder surface has become noticeably thinner compared with the lower Rayleigh number cases, which means the local heat flux from the cylinder has increased substantially. These features are consistent with the findings of Demirdžić and Lilek [15] and Shu et al. [42].

At $Ra = 5 \times 10^6$ (Figure 8d), the trends already established at $Ra = 10^6$ are pushed further but no qualitatively new feature appears in the temperature field. The plume above the cylinder is narrower and more sharply defined, and the isotherm packing immediately above the top of the cylinder is the densest seen in the steady regime. The horizontal spread of the plume along the top wall is also more compact, with the warm fluid traveling further down the side walls before mixing with the cold return flow. The S-shaped distortion on the lateral sides of the cylinder is more pronounced, but the contours on the two sides of the cavity remain mirror images of each other to graphical accuracy. The stratified pool below the cylinder grows further and the lower third of the cavity is filled with widely spaced nearly horizontal isotherms that change very little with Rayleigh number once Ra passes 10^6.

5.2.2 Streamlines

The streamline patterns for the four Rayleigh numbers of the steady regime are presented in Figure 9. Streamlines give a direct picture of the fluid motion inside the cavity, and the way they change with rising Rayleigh number brings out the steady strengthening and rearrangement of the buoyancy driven flow.

For $Ra = 10^4$ (Figure 9a) the flow is made up of two symmetric, counter rotating recirculation cells placed on either side of the vertical centre line. Each cell takes up nearly half of the annular space lying between the cylinder and the cavity wall. The fluid moves along the hot cylinder surface, travels towards the top of the cavity, comes down along the cold side wall, and returns to the bottom of the cylinder to close the loop. Being smooth and evenly spaced, the streamlines reflect a gentle and orderly circulation. Each main cell carries two separate centres of recirculation, one in its upper part and one in its lower part, which is typical of the rather shallow flow at this Rayleigh number. The peak stream function is only about 1.0 (Table 3), so the circulation at this stage stays weak.

At $Ra = 10^5$ (Figure 9b) the two principal cells gain strength and their inner structure becomes simpler. The pair of recirculation centres that stayed apart in each cell at $Ra = 10^4$ now join into a single, well defined vortex core seated in the upper part of the cell. With the maximum stream function climbing to about 8.35, nearly eight times as much fluid is set into circulation in each cell as at $Ra = 10^4$. Near the cylinder surface and over the top portion of the cavity the streamlines pack more closely, which is a mark of the higher velocities prevailing in those regions. A thin stagnation zone shows up below the cylinder along the vertical centre line, where the two cells come together and the downward flow merges. The bilateral symmetry of the flow is held well at this Rayleigh number.

Once the Rayleigh number reaches 10^6 (Figure 9c) the flow grows more vigorous. The maximum stream function moves up to about 24.2 and the peak velocity magnitude touches roughly 267 (Table 3). The two primary cells now cover a larger share of the cavity and their centres have shifted higher up. One notable change at this Rayleigh number is the appearance of two small, sharply defined corner vortices at the lower wall, one sitting in each bottom corner. These eddies form because the strong downward stream along the side walls, on reaching the cavity floor, is unable to turn smoothly and instead sets up a local recirculation in the bottom region. Over the cylinder the streamlines are drawn very tightly along the vertical centre line, marking a strong and narrow updraft that is the kinematic partner of the thermal plume seen in the isotherms. Beneath the cylinder the two cells meet at the bottom centre line, where the flow gathers into a thin downward stream and then splits once more to feed the two primary cells. The flow pattern as a whole stays symmetric about the vertical centre line, and these features agree with what has been reported for similar enclosure problems in the literature [15, 32].

At $Ra = 5 \times 10^6$ (Figure 9d) the same two cell topology is retained, but the flow is far more energetic. In absolute terms the maximum stream function reaches about 35 and the peak velocity is close to 624. The vortex cores of the two main cells drift still further into the upper third of the cavity, so that the lower half is left mostly to slowly recirculating fluid. The corner eddies near the lower wall, which made their

first appearance at $Ra = 10^6$, are now larger and more clearly resolved, and a thin secondary structure between these corner vortices and the bottom of the cylinder also becomes visible. The boundary layer over the cylinder surface is plainly thinner than at $Ra = 10^6$, and on either side of the plume the streamlines fold into a narrow column above the cylinder before spreading out along the top wall.

5.2.3 Nusselt Number Variation

The rising plume, the thinning thermal boundary layer on the cylinder, and the increasingly stratified pool at the bottom of the cavity all leave their mark on the rate at which heat is transferred from the cylinder to the cavity walls. To make this connection quantitative, the surface averaged Nusselt number on the cylinder $\overline{Nu}_{\mathrm{cyl}}$, the wall averaged values $\overline{Nu}_w$ on each cavity face, and the local distribution $Nu(\theta)$ around the cylinder are examined.

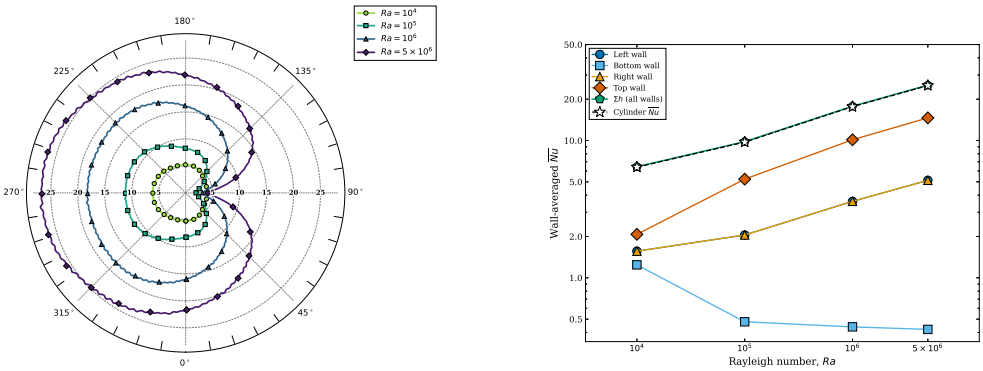
Validation.

The present surface averaged cylinder Nusselt number $\overline{Nu}_{\mathrm{cyl}}$ is compared with three independent benchmarks [2, 17, 27] at the four Rayleigh numbers for which reference data are available (10^4, 10^5, 10^6, and 10^7). The agreement is within 1.6% in every case and falls below 1% at $Ra = 10^6, 10^7$. This level of agreement is taken as confirmation that the body conforming grid resolves the thermal boundary layer on the cylinder adequately. The detailed graphical comparison together with the global Nusselt-Rayleigh correlation is deferred to Section 5.4.3, where the steady values are plotted alongside the unsteady ones so that a single fit can be performed on the full range of Rayleigh number.

Local distribution on the cylinder.

The angular distribution of the local Nusselt number around the cylinder, $Nu(\theta)$, is shown in Figure 10a, with $\theta = 0^\circ$ at the bottom of the cylinder and θ increasing in the counter clockwise direction. All four cases share two qualitative features, a deep minimum near the lateral generators of the cylinder ($\theta \approx 90^\circ$ and $\theta \approx 270^\circ$, where the gap between the cylinder and the side wall is thinnest and the boundary layer separates), and a broad maximum in the upper half ($\theta > 180^\circ$) where the buoyant plume is born.

The quantitative gap between these extrema widens with Ra. At $Ra = 10^4$ the profile is shallow and $Nu_{\max} = 6.17$ at $\theta_{\mathrm{peak}} = 275.4^\circ$ and $Nu_{\min} = 4.01$ at the sides which gives a peak to valley ratio of about 1.5 with a circumferential mean of 5.09. By $Ra = 10^5$ the lateral minimum collapses to 1.91 while the upper peak climbs to 11.31 (still at $\theta_{\mathrm{peak}} = 275.4^\circ$) and the peak to valley ratio is now close to six. At $Ra = 10^6$ the peak reaches 18.45 and the minimum recovers to 3.08. The recovery of the lateral minimum is driven by the bottom corner eddies (Figure 9c) which begin to feed cooler fluid back across the lower flank of the cylinder. At $Ra = 5 \times 10^6$ the peak rises further to 27.06 and the minimum is 4.09, with θ_{peak} remaining pinned at 275.4°. The standard deviation of $Nu(\theta)$ rises monotonically from 0.68 at $Ra = 10^4$ to 4.70 at $Ra = 10^6$ and then to 5.99 at $Ra = 5 \times 10^6$, confirming that the heat flux becomes increasingly non uniform around the circumference of the cylinder as Ra is increased.



(a) Polar distribution of the local Nusselt number $Nu(\theta)$ on the cylinder.

(b) Wall averaged Nusselt numbers on the four cavity walls and the cylinder.

Fig. 10: Local and wall resolved heat transfer for $10^4 \leq Ra \leq 5 \times 10^6$, $Pr = 0.71$.

Wall-averaged heat flux.

Figure 10b shows the wall averaged Nusselt number on each of the four cold walls together with the cylinder value $\overline{Nu}_{\mathrm{cyl}}$. The cylinder curve sits above all four wall curves at every Rayleigh number, as it must by global energy balance: the heat released by the cylinder is shared between the four walls. At $Ra = 10^4$ the four wall averaged values lie close together: $\overline{Nu}_{\mathrm{top}} = 2.07$, $\overline{Nu}_{\mathrm{left}} = \overline{Nu}_{\mathrm{right}} = 1.56$, and $\overline{Nu}_{\mathrm{bot}} = 1.24$. Expressed as fractions of the total wall heat, this corresponds to about 32%, 24%, 24% and 19% respectively, the near uniform partition expected of a conduction dominated transport.

As the Rayleigh number grows the four curves fan out. The top wall climbs steeply, with $\overline{Nu}_{\mathrm{top}}$ taking the values 5.23, 10.13 and 14.62 at $Ra = 10^5$, 10^6 and 5×10^6, and its share of the total wall heat rising to 53%, 57% and 58%. The two side walls remain equal to within numerical precision and grow as $\overline{Nu}_{\mathrm{side}} = 2.05 \rightarrow 3.61 \rightarrow 5.13$, with each side wall absorbing close to 20% of the heat at all Rayleigh numbers above 10^4. The bottom wall, by contrast, falls off the page: $\overline{Nu}_{\mathrm{bot}}$ decreases from 1.24 at $Ra = 10^4$ to 0.48, 0.44 and 0.42 at the higher Rayleigh numbers, and its share of the load collapses to less than 2% at $Ra = 5 \times 10^6$. Two physical effects drive this redistribution. The first is the vertical plume, which delivers most of the hot fluid directly to the upper wall. The second is the stratified pool of fluid that builds up below the cylinder as Ra increases, a feature already evident in the widely spaced lower isotherms of Figures 8c and 8d. The bottom wall therefore exhibits the somewhat counter intuitive behaviour of a Nusselt number that *decreases* as the Rayleigh number rises.

5.3 Transition and onset of unsteadiness

The present section follows the cylinder averaged Nusselt number $Nu_{\mathrm{cyl}}(t)$ across the loss of stability and into the time periodic regime, using the time histories at all eight

Rayleigh numbers studied in this work ($Ra = 10^4$, 10^5, 10^6, 5×10^6, 7.5×10^6, 10^7, 2.5×10^7 and 5×10^7) and the associated regime transition diagram.

Time histories at all the Rayleigh numbers.

The eight time histories of $Nu_{\mathrm{cyl}}(t)$ are shown in the lower rows of Figure 11 and span seven orders of magnitude in fluctuation amplitude. At $Ra = 10^4$ (Figure 11b) the sample standard deviation is $\sigma(Nu_{\mathrm{cyl}}) = 3.79 \times 10^{-7}$, essentially the iterative solver tolerance. At $Ra = 10^5$ and $Ra = 10^6$ (Figures 11c and 11d) σ rises to 1.0×10^{-5} and 3.82×10^{-5} respectively. These values are still less than $10^{-3}\%$ of the mean, but they are now above the solver noise floor. A periodic oscillation of amplitude $\sim 5 \times 10^{-5}$ becomes visible in the magnified trace at $Ra = 10^6$, and a similar but weaker oscillation is present at $Ra = 10^5$. The behaviour at $Ra = 5 \times 10^6$ (Figure 11e) continues this trend but is sharper and $\sigma = 1.47 \times 10^{-4}$ which is almost four times the value at $Ra = 10^6$. The magnified trace shows a small periodic-like envelope just above the solver noise floor. Read in isolation this rise might still be interpreted as a smooth continuation of the lower Rayleigh number trend, but read in combination with the kinematic asymmetry between $\psi_{\max}$ and $|\psi_{\min}|$ already noted in the streamline analysis, it identifies the system at $Ra = 5 \times 10^6$ as no longer a perfect fixed point.

The four traces at $Ra = 7.5 \times 10^6$, 10^7, 2.5×10^7 and 5×10^7 are qualitatively different. At $Ra = 7.5 \times 10^6$ (Figure 11f) the signal is a nearly clean periodic oscillation around the time mean $\overline{Nu}_{\mathrm{cyl}} = 27.185$ with $\sigma(Nu_{\mathrm{cyl}}) = 2.80 \times 10^{-1}$. The cycle to cycle amplitude is approximately constant and the peaks are evenly spaced in time. At $Ra = 10^7$ (Figure 11g) the trace remains oscillatory and the mean rises to $\overline{Nu}_{\mathrm{cyl}} = 29.076$ with $\sigma = 3.41 \times 10^{-1}$, but the peak to peak amplitude of consecutive cycles is no longer constant and a slow modulation of the envelope is visible. The signal at $Ra = 2.5 \times 10^7$ (Figure 11h) has $\sigma = 4.93 \times 10^{-1}$ and shows pronounced amplitude beating, with consecutive cycles varying in both amplitude and shape and a longer modulation period superimposed on the basic oscillation. By $Ra = 5 \times 10^7$ (Figure 11i) no clear periodicity is left in the trace. The instantaneous Nu_{cyl} jumps erratically between about 40.8 and 46.5 about its mean of $\overline{Nu}_{\mathrm{cyl}} = 43.090$, the standard deviation has climbed to $\sigma = 6.15 \times 10^{-1}$, and the signal now carries energy across a wide span of timescales. Taken in order, the four signals lay out their own story. A clean limit cycle at $Ra = 7.5 \times 10^6$ slowly gives way to a broad-band, irregular trace at $Ra = 5 \times 10^7$. The path is clear enough: a periodic state first, then a quasi-periodic stage in between, and finally chaos at the end. The detailed classification that confirms this picture is provided by the energy spectral densities of Section 5.4.4 and by the Poincaré maps of Section 5.4.5.

Regime transition diagram and critical Rayleigh number.

The top panel of Figure 11 collects the time mean $\overline{Nu}_{\mathrm{cyl}}$ (filled circles, left axis) and the standard deviation $\sigma(Nu_{\mathrm{cyl}})$ (orange squares, right axis) at all the eight Rayleigh numbers. The mean Nusselt number grows smoothly across the full range without any visible break, rising from 6.40 at $Ra = 10^4$ to 43.09 at $Ra = 5 \times 10^7$. The standard deviation tells a very different story. From $Ra = 10^4$ to $Ra = 5 \times 10^6$, σ rises gently from 3.79×10^{-7} to 1.47×10^{-4}, an increase of less than two orders of magnitude

spread over nearly three decades of Ra. Between $Ra = 5 \times 10^6$ and $Ra = 7.5 \times 10^6$, however, σ jumps from 1.5×10^{-4} to 2.8×10^{-1}, an increase of more than three orders of magnitude over a Rayleigh number ratio of only 1.5. Beyond $Ra = 7.5 \times 10^6$ the growth of σ is again smooth, rising by only a factor of about 2.2 as Ra is raised by a factor of nearly seven.

The change of slope of σ on the axes therefore identifies the critical Rayleigh number for the onset of unsteadiness as

$$5 \times 10^6 \; < \; Ra_c \; < \; 7.5 \times 10^6. \tag{45}$$

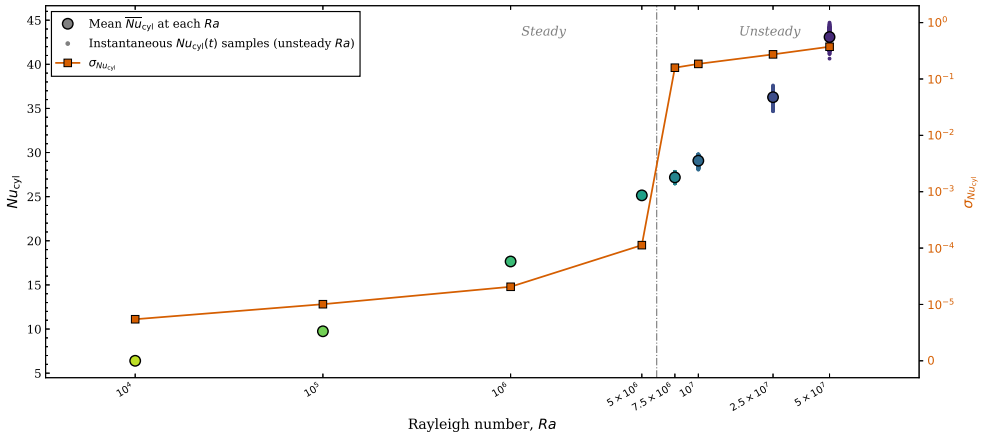
The coverage of the Rayleigh number axis used here is too coarse to localize Ra_c more precisely closing this bracket would require simulations at intermediate values. However, the estimate is consistent with the range $Ra_c \sim 10^6$ to 10^7 reported by Wang et al. [47] for unsteady plume dynamics around a heated cylinder in a confined enclosure. It is also higher than the value that would have been obtained if the stream function on the cylinder had been clamped to zero, as in the earlier study of Dutta et al. [17], since that constraint suppresses the very asymmetric mode that drives the regime transition seen here.

5.4 Unsteady Results ($Ra \geq 7.5 \times 10^6$)

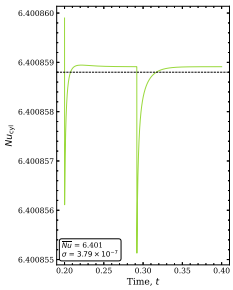
5.4.1 Instantaneous flow structure

The instantaneous fields are the direct way of showing that the symmetric steady state has been replaced by a state that varies in both space and time. Two Rayleigh numbers are reported in this subsection: $Ra = 10^7$, which represents the system shortly after the onset of unsteadiness, and $Ra = 5 \times 10^7$, which represents the chaotic state (discussed in Section 5.4.4 and 5.4.5) at the upper end of the range studied. The intermediate cases $Ra = 7.5 \times 10^6$ and 2.5×10^7 display the same qualitative behaviour at intermediate strength and not shown because of compactness.

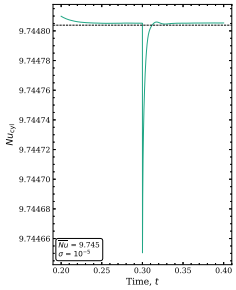
Figures 12 and 14 show the instantaneous isotherms and streamlines at $Ra = 10^7$ at four times during one period of the oscillation. The first observation is that no snapshot is symmetric about the vertical centre line of the cavity. In Figure 12a the plume above the cylinder leans slightly to the left and a small closed isotherm contour, the thermal trace of a detached warm pocket, sits in the upper right corner. By Figure 12b the plume has swung to the opposite side and a curl shaped warm pocket detaches from the cylinder cap and travels along the upper right region of the cavity. The streamline plots in Figure 14 tell the kinematic side of the same picture. The two main recirculation cells are visibly unequal in size at every instant, and the small secondary vortices that sit between the main cells and the corners of the cavity appear and vanish between snapshots. The number of distinct closed streamline loops therefore changes with time and is not just a question of fixed structures shifting position. The thermal boundary layer wrapped around the cylinder remains thin at every instant, but the arc along which it is densely packed alternates between the left and right halves of the cylinder in step with the swing of the plume. At $Ra = 10^7$ the lower stratified pool below the cylinder is still intact. This pool was a robust feature of every steady case, and even



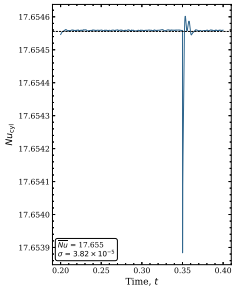
(a) Regime transition diagram.



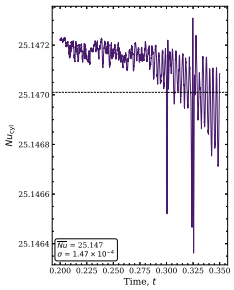
(b) $Ra = 10^4$



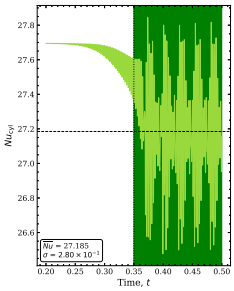
(c) $Ra = 10^5$



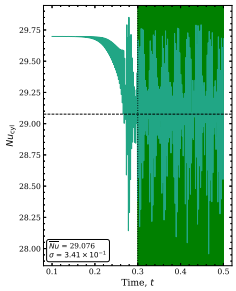
(d) $Ra = 10^6$



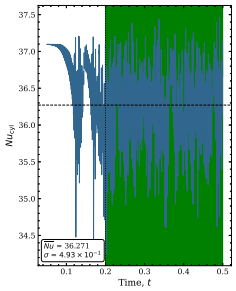
(e) $Ra = 5 \times 10^6$



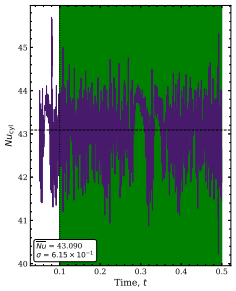
(f) $Ra = 7.5 \times 10^6$



(g) $Ra = 10^7$



(h) $Ra = 2.5 \times 10^7$



(i) $Ra = 5 \times 10^7$

Fig. 11: Regime transition diagram of the cylinder Nusselt number (Nu_{cyl}) together with the time histories at all the eight Rayleigh numbers.

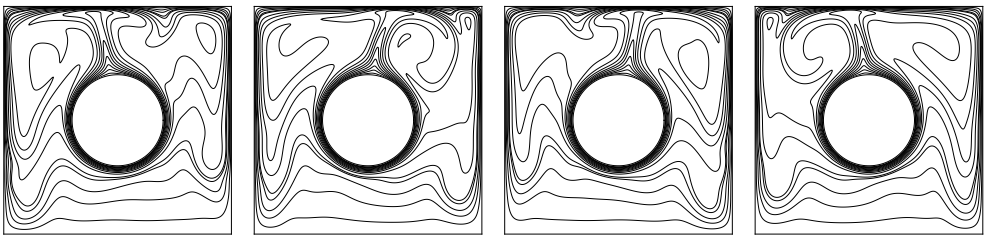
here it is disturbed only near its upper surface, where the descending side-wall jets feed into the bulk.

Figures 13 and 15 show the instantaneous isotherms and streamlines at $Ra = 5 \times 10^7$. The character of the flow has now changed in a way that is not simply a stronger version of what was seen at $Ra = 10^7$. The plume above the cylinder is no longer a coherent rising column. In each isotherm snapshot the plume appears as a sequence of detached warm blobs that rise, bend, and shed in the upper part of the cavity. Closed isotherm loops, which were a rare and short lived feature at $Ra = 10^7$, are present in every snapshot at $Ra = 5 \times 10^7$ and occur on both sides of the cavity. The lower stratified pool is preserved to a very small extent, close to the bottom wall but in slight wavy nature. Wavy distortions of the lower isotherms reach roughly halfway up the cavity, which shows that the high speed side wall jets are now energetic enough to pump cold fluid into the bulk on every cycle rather than to let it settle quietly at the bottom. The streamlines in Figure 15 are reshaped even more sharply. Any one snapshot carries between five and eight distinct vortex cores. Their sizes cover a wide span, from large primary cells that fill much of the cavity down to small detached eddies the size of only a few percent of the cavity area. The smaller cores no longer sit in the corners or along the side walls. They show up as isolated closed streamline loops inside the cavity itself, and they shift position from one snapshot to the next. The instantaneous topology of the streamline pattern therefore changes qualitatively between snapshots, not only quantitatively. This is the kinematic signature of a chaotic state rather than of a simple periodic one.

The geometric and thermal boundary conditions of the problem are perfectly symmetric about the vertical centre line, so the asymmetry observed at any single instant is not the consequence of a permanent symmetry breaking of the system. It is rather the consequence of the system spending time in a continuous sequence of asymmetric states whose left and right mirror images are equally accessible. The high flux arc of the cylinder, that is, the section of the cylinder surface across which the thermal boundary layer is most densely packed, alternates between the left and right halves of the cylinder as the plume swings. All observed instantaneous snapshot therefore reports a strongly asymmetric local Nusselt number distribution around the cylinder, with the peak position varying in time. The number of closed streamline loops is itself a time dependent quantity. At $Ra = 10^7$ it ranges between three and five from one snapshot to the next, while at $Ra = 5 \times 10^7$ it ranges between five and eight. All of these instantaneous asymmetries are shown in average isotherms and streamlines to a flow that is approximately symmetric about the vertical centre line, and the structure of the steady regime is largely recovered in the mean.

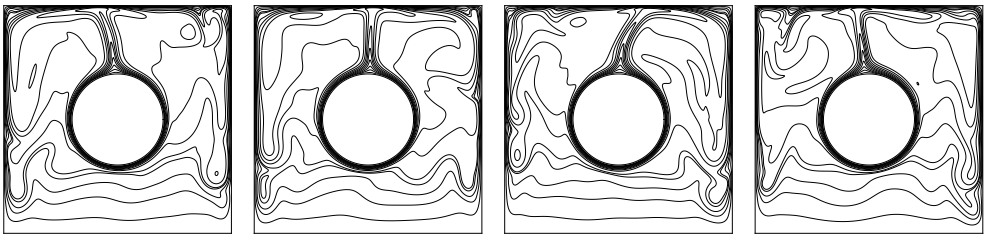
5.4.2 Time averaged flow structure

The instantaneous snapshots showed a flow whose spatial structure varies continuously in time. When these fields are averaged over a sufficiently long time window, a clear mean topology emerges that is the natural extension of the steady state. This subsection reports the time averaged isotherms and streamlines for all four unsteady Rayleigh numbers, together with the peak instantaneous flow quantities and the time averaged Nusselt numbers summarized in Table 4.



(a) $t = 1.0000$ (b) $t = 1.0011$ (c) $t = 1.0023$ (d) $t = 1.0034$

Fig. 12: Instantaneous isotherms for $Ra = 10^7$, $Pr = 0.71$, at four times during one period of the oscillation.



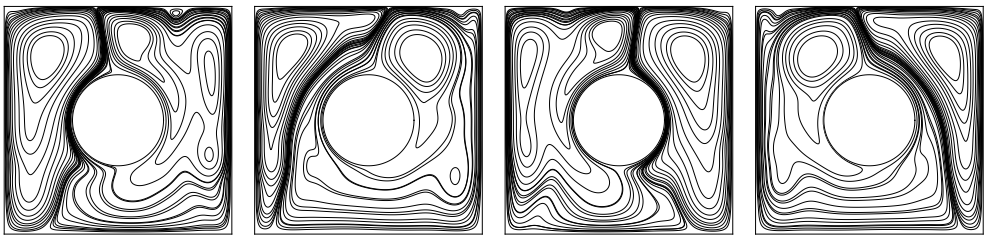
(a) $t = 0.4750$ (b) $t = 0.4755$ (c) $t = 0.4760$ (d) $t = 0.4765$

Fig. 13: Instantaneous isotherms for $Ra = 5 \times 10^7$, $Pr = 0.71$, at four times during one period of the oscillation.

Across the unsteady range, the peak stream function magnitude $\psi_{\max}$ grows from about 46.7 at $Ra = 7.5 \times 10^6$ to about 83.7 at $Ra = 5 \times 10^7$, a factor of 1.8. The peak vertical velocity climbs from $|v|_{\max} = 618$ to 1618, a factor of 2.6, and the peak horizontal velocity from $|u|_{\max} = 564$ to 1523, a similar factor of 2.7. For reference, the largest steady case at $Ra = 5 \times 10^6$ had $\psi_{\max} = 34.6$ and $|v|_{\max} = 624$, so the transition into the unsteady regime is accompanied by an immediate jump of about 30 to 50 percent in the peak kinematic quantities. The energy balance between the cylinder and the cavity walls remains closed to within numerical accuracy at every unsteady Ra, with $\overline{Nu}_{\mathrm{cyl}}$ and $\overline{Nu}_{\mathrm{encl}}$ differing by less than 0.6% in the worst case.

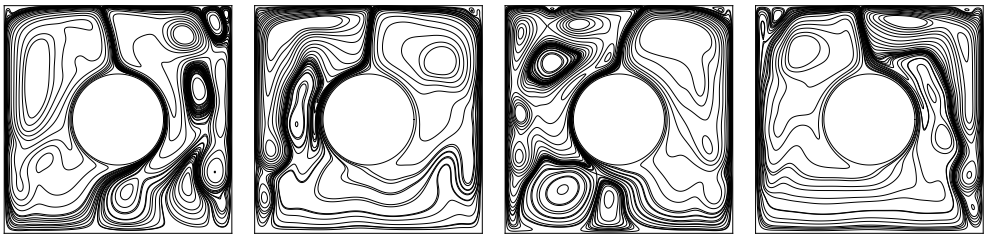
Isotherms

The time averaged isotherms are shown in Figure 16 for the four Rayleigh numbers. The most striking feature is that the bilateral symmetry of the mean field is recovered to the eye at every Ra, in clear contrast to the strongly asymmetric instantaneous snapshots of Figures 12 and 13. The averaged plume sits directly above the cylinder and rises in a narrow column to impinge on the cold top wall. Two cold lobes descend on either side of the plume into the upper half of the cavity. The lower half of the cavity is filled with stratified, nearly horizontal isotherms. The thermal boundary layer



(a) $t = 1.0000$ (b) $t = 1.0011$ (c) $t = 1.0023$ (d) $t = 1.0034$

Fig. 14: Instantaneous streamlines for $Ra = 10^7$, $Pr = 0.71$, at four times during one period of the oscillation.



(a) $t = 0.4750$ (b) $t = 0.4755$ (c) $t = 0.4760$ (d) $t = 0.4765$

Fig. 15: Instantaneous streamlines for $Ra = 5 \times 10^7$, $Pr = 0.71$, at four times during one period of the oscillation.

wrapped around the cylinder is thin at every Ra, with isotherms tightly packed against the cylinder surface.

The Rayleigh number trend is monotonic. At $Ra = 7.5 \times 10^6$ (Figure 16a) the plume is comparatively wide and the cold lobes occupy only the upper corners. The lower stratified pool is thick and its isotherms are essentially horizontal, which is the signature of a near conduction state in the lower cavity. At $Ra = 10^7$ (Figure 16b) the plume narrows and the cold lobes extend further down along the side walls. At $Ra = 2.5 \times 10^7$ (Figure 16c) the plume is a slender column and the cold lobes fill the upper half of the cavity, descending almost to the height of the cylinder centre on either side. By $Ra = 5 \times 10^7$ (Figure 16d) the plume is thinner still, the cold lobes have grown further, and the lower isotherms now show clear wave like distortions that were absent at lower Ra. These distortions are the mean trace of the wavy lower isotherms seen in the instantaneous snapshots and they indicate that the side wall jets at this Rayleigh number have begun to pump cold fluid into the stratified pool on every cycle. The progressive thinning of the thermal boundary layer wrapped around the cylinder over this range is consistent with the rise of the time averaged cylinder Nusselt number reported in Section 5.4.3.

Streamlines

The time averaged streamlines are shown in Figure 17. The two cell topology of the steady regime is preserved in the mean at every unsteady Ra. Two large counter rotating cells fill the cavity on either side of the vertical centre line, with their vortex cores located in the upper third of the cavity. Fluid rises along the hot cylinder surface, sweeps across under the cold top wall, descends along the cold side walls, and returns toward the cylinder along the bottom of the cavity. There is no qualitative change in the mean streamline topology between $Ra = 7.5 \times 10^6$ and $Ra = 5 \times 10^7$ but the strength of the circulation and the position of the vortex cores changes. As Ra rises across the range, the peak stream function on each side grows from 46.7 to 83.7 and the vortex cores migrate slightly upward and toward the side walls.

The small recirculation that occupied the bottom corners of the cavity in the steady solutions at $Ra = 10^6$ and 5×10^6 is no longer visible as a fixed structures in any of the averaged unsteady fields. At every unsteady Ra the bottom corners are part of the main cells, with no closed streamline loop sitting in either corner. The instantaneous snapshots of Figures 14 and 15 make it clear that bottom corner eddies do exist at every instant but these eddies have lost a fixed position and are smeared out of the time average. A thin band of nearly horizontal streamlines remains immediately above the bottom wall which is the kinematic counterpart of the stratified lower pool seen in the isotherms.

Almost steady appearance of the averaged fields

The averaged isotherms and streamlines of Figures 16 and 17 look remarkably like steady state solutions. The bilateral symmetry is restored, the plume is stationary and well defined, and the recirculation cells are smooth and orderly. This appearance is somewhat deceptive. The instantaneous snapshots make it clear that the underlying flow at every instant is asymmetric, contains a varying number of vortex cores, and at $Ra = 5 \times 10^7$ is no longer dominated by a single coherent plume. The reason that the time average looks symmetric is geometric in origin. The governing equations and the boundary conditions of the problem are invariant under reflection about the vertical centre line, so for every instantaneous state S that the system visits during the simulation, the mirror image state S' is also an admissible state of the system. Over a long enough time window the trajectory visits both equally often, and the time average lies on the symmetry plane of the underlying dynamical system. This restoration of symmetry through statistical averaging is a generic feature of fully developed chaotic flow in a geometrically symmetric configuration [45, 47]. The fact that the averaged fields look almost steady should therefore not be read as evidence that the underlying flow is steady.

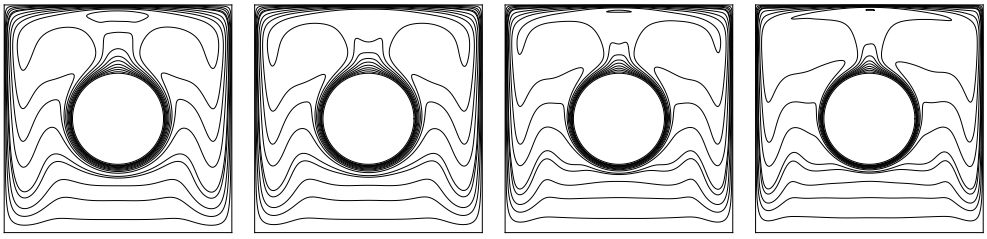
5.4.3 Heat transfer characteristics

Local distribution on the cylinder

The time averaged local Nusselt number around the cylinder, $Nu(\theta)$, is shown for the four unsteady Rayleigh numbers in Figure 19a. The angle convention follows in such a way that $\theta = 0^\circ$ at the bottom of the cylinder with θ increasing in the counter clockwise

Table 4: Flow statistics for unsteady natural convection around a heated cylinder placed inside a square cavity ($Pr = 0.71$).

Quantity	$Ra = 7.5 \times 10^6$	$Ra = 10^7$	$Ra = 2.5 \times 10^7$	$Ra = 5 \times 10^7$
$\psi_{\max}$	46.692	55.389	69.464	83.747
$\psi_{\min}$	-47.317	-55.309	-70.311	-83.133
$\lvert u\rvert_{\max}$	563.9	622.0	1044.6	1523.0
$\lvert v\rvert_{\max}$	617.6	719.6	1142.9	1618.4
$\overline{Nu}_{\text{cyl}}$	27.185	29.076	36.271	43.090
$\overline{Nu}_{\text{encl}}$	27.346	29.240	36.399	43.147

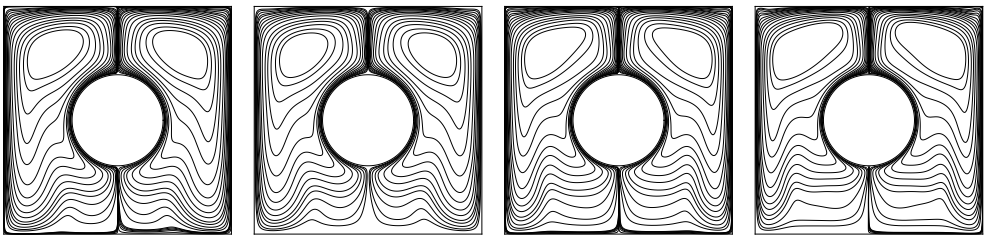


(a) $Ra = 7.5 \times 10^6$ (b) $Ra = 10^7$ (c) $Ra = 2.5 \times 10^7$ (d) $Ra = 5 \times 10^7$

Fig. 16: Time averaged isotherms of natural convection around a heated cylinder placed in a square cavity for $7.5 \times 10^6 \leq Ra \leq 5 \times 10^7$, $Pr = 0.71$.

direction. The four curves share the qualitative shape established in the steady regime, with a broad maximum on each side of the cylinder cap and two lateral minima where the cold side wall is closest and the boundary layer separates. As the Rayleigh number is increased, the maxima and the minima both grow but at different rates. The peak value rises from $Nu_{\max} = 29.56$ at $Ra = 7.5 \times 10^6$ to 47.07 at $Ra = 5 \times 10^7$, a factor of 1.6, while the minimum value rises only from 5.61 to 6.59, a factor of 1.2. The lateral minima therefore become relatively flatter as the Rayleigh number is increased which is consistent with the chaotic mixing of the unsteady regime redistributing thermal energy around the cylinder more efficiently than steady laminar convection and smoothing the cold spots on the lateral generators without diminishing the peak heat flux above the cylinder.

At $Ra = 7.5 \times 10^6$, 10^7, and 2.5×10^7 the time averaged peak sits at $\theta_{\text{peak}} = 275.35°$, exactly the same value reported for every steady Rayleigh number in Section 5.2.3. At $Ra = 5 \times 10^7$, however, the peak shifts to $\theta_{\text{peak}} = 243.07°$, more than 30° away from the position pinned at lower Ra. Two interpretations of this shift are possible. The first is that the chaotic attractor at $Ra = 5 \times 10^7$ is not perfectly symmetric within the finite time window used for averaging here, and that the apparent shift is a sampling issue that would relax to 270° on a much longer record. The second is that



(a) $Ra = 7.5 \times 10^6$ (b) $Ra = 10^7$ (c) $Ra = 2.5 \times 10^7$ (d) $Ra = 5 \times 10^7$

Fig. 17: Time averaged streamlines of natural convection around a heated cylinder placed in a square cavity for $7.5 \times 10^6 \leq Ra \leq 5 \times 10^7$, $Pr = 0.71$.

the shift is a genuine feature of the attractor at this Rayleigh number, possibly linked to the strong thermal-plume detachment from the cylinder cap and to the long lived asymmetric plume configurations seen in the instantaneous snapshots of Figure 13.

Wall averaged heat flux distribution

The wall averaged Nusselt numbers on the four cavity walls and on the cylinder are plotted as functions of Rayleigh number in Figure 19b. The cylinder average $\overline{Nu}_{\mathrm{cyl}}$ and the total wall load $\overline{Nu}_{\mathrm{encl}}$ collapse onto one another at every Rayleigh number to within the energy balance error of less than 0.6%, which confirms that the time averaged heat balance is closed. The top wall carries the largest fraction of the load at every Rayleigh number, with $\overline{Nu}_{\mathrm{top}}$ growing from 14.88 at $Ra = 7.5 \times 10^6$ to 23.85 at $Ra = 5 \times 10^7$. Expressed as a fraction of the total wall heat, the top wall absorbs 54%, 54%, 55%, and 55% respectively across the four unsteady cases, an almost constant share that continues smoothly from the steady regime. The two side walls are indistinguishable to within the resolution of the plot, with values that grow from about 6.0 at $Ra = 7.5 \times 10^6$ to about 9.5 at $Ra = 5 \times 10^7$ and a near constant share of about 22% each.

The bottom wall shows the most striking behaviour. $\overline{Nu}_{\mathrm{bot}}$ decreases as the Rayleigh number is increased, from 0.38 at $Ra = 7.5 \times 10^6$ to 0.28 at $Ra = 5 \times 10^7$, even though the cylinder Nusselt number is rising by a factor of 1.6 over the same range. The share of the bottom wall in the total wall load therefore falls from 1.4% at $Ra = 7.5 \times 10^6$ to 0.6% at $Ra = 5 \times 10^7$. This continues the anomalous trend already documented in the steady regime where $\overline{Nu}_{\mathrm{bot}}$ was shown to fall with Rayleigh number even as the global cylinder Nusselt number was rising. As the Rayleigh number is raised, the lower part of the cavity becomes more strongly stratified and the descending side wall jets, which are the source of cold fluid for the bottom wall, are increasingly absorbed into the bottom corner vortices before they reach the lower boundary layer. In the unsteady regime the bottom corner vortices are no longer fixed structures but transient corner eddies (Figure 15) on time averaging they still act as an effective barrier between the cold side wall jet and the bottom wall.

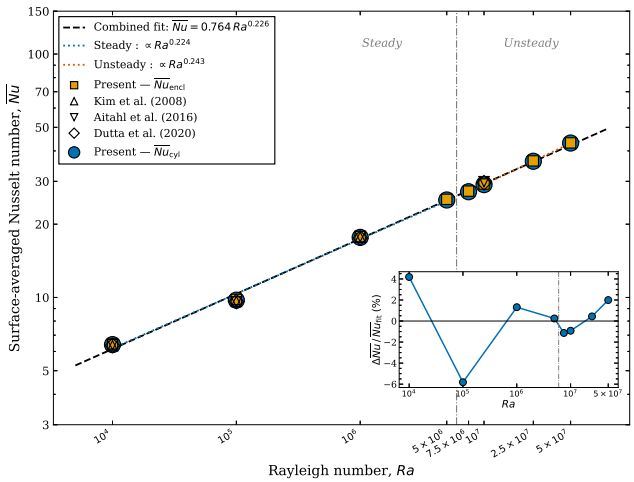


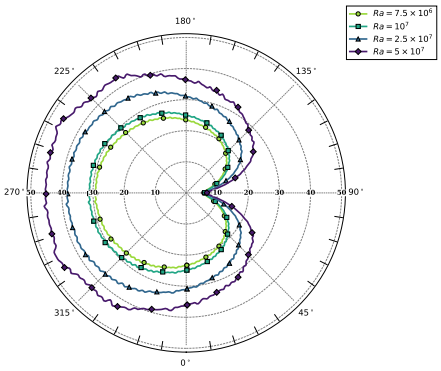
Fig. 18: Surface averaged Nusselt number on the heated cylinder as a function of Rayleigh number across the full range $10^4 \leq Ra \leq 5 \times 10^7$, $Pr = 0.71$ and Inset depicting relative deviation.

Global Nusselt-Rayleigh correlation

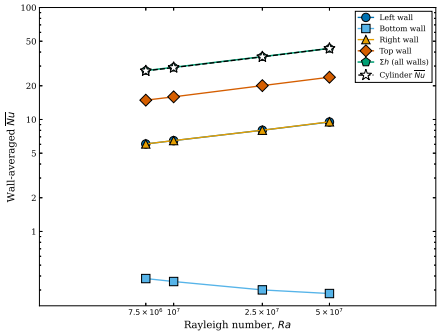
A single power law of the form $\overline{Nu}_{\mathrm{cyl}} = C\,Ra^n$ is now fitted to all eight time averaged cylinder Nusselt numbers, four from the steady regime ($10^4 \leq Ra \leq 5 \times 10^6$) and four from the unsteady regime ($7.5 \times 10^6 \leq Ra \leq 5 \times 10^7$). The combined least squares fit returns

$$\overline{Nu}_{\mathrm{cyl}} \;=\; 0.764\,Ra^{0.226}, \tag{46}$$

with a residual scatter that stays within 6% at every data point as shown in the inset of Figure 18. Fitted on its own, the steady branch gives $n_{\mathrm{steady}} = 0.224$ and the unsteady branch gives $n_{\mathrm{unsteady}} = 0.243$, a steepening of about 0.02 across the transition. The reason behind this small change is simple. In the unsteady regime two contributions add up in the time-averaged heat transport. The first comes from the mean flow and scales like the steady laminar boundary-layer transport, with n close to 1/4. The second comes from the fluctuating field, and grows faster with Ra because the fluctuation amplitude itself grows with Ra. The two together give an effective exponent slightly above 1/4, which is what the unsteady fit returns. Both exponents sit between the classical laminar boundary-layer prediction $n = 1/4$ [7] and the Castaing soft-turbulence scaling $n = 2/7 \approx 0.286$ [10]. This middle position fits the picture that the flow at the upper end of the range is no longer purely boundary-layer dominated, but has also not yet reached fully developed turbulence. The combined exponent (0.226) is closer to the steady value than to the unsteady value because the steady range spans nearly three decades of Ra while the unsteady range spans less than one decade, so the steady points dominate the least squares fit.



(a) Polar distribution of the local Nusselt number $Nu(\theta)$ on the cylinder.



(b) Wall averaged Nusselt numbers on the four cavity walls and the cylinder.

Fig. 19: Local and wall resolved heat transfer for $7.5 \times 10^6 \leq Ra \leq 5 \times 10^7$, $Pr = 0.71$.

5.4.4 Energy spectral density

The regime transition diagram placed the cylinder averaged Nusselt number on a continuous path from a clean limit cycle at $Ra = 7.5 \times 10^6$ to a broad band irregular trace at $Ra = 5 \times 10^7$. That diagnostic is a single scalar averaged over the cylinder surface. It therefore says nothing about where in the cavity the unsteadiness lives, or about the frequency content carried by the local velocity field. The present subsection answers both questions using the energy spectral density (ESD) of the velocity fluctuation vector $\mathbf{u}' = (u', v')$ recorded at the eleven probes P1-P11 defined in Section 2.1.

Of the eleven probes, three are retained here for the discussion. Probe P3 at $(x/L, y/L) = (0.5, 0.95)$ sits directly in the plume impingement region above the cylinder and records the strongest signal at every Rayleigh number. Probe P9 at $(0.15, 0.5)$ sits on the side wall descending jet on the left of the cylinder. Probe P11 at $(0.5, 0.15)$ samples the lower stratified pool that the steady regime analysis identified as the quietest region of the cavity. All other probes convey the results similar to those of three chosen points so they are not shown for compactness.

Frequencies are reported in the non dimensional form f^*. The spectrum $E^*(f^*)$ is computed from the sum of the auto-spectra of the two velocity fluctuation components and is normalized so that its integral over f^* equals the time averaged turbulent kinetic energy $E^*_{\mathrm{TKE}} = \frac{1}{2}\overline{(u'^2 + v'^2)}$ at the corresponding probe.

At $Ra = 7.5 \times 10^6$ (Figure 20, $Ra = 7.5 \times 10^6$ row) the spectrum at P3 is dominated by a single sharp peak at $f^* \approx 183$ together with a comb of equally spaced harmonics that extend up to $f^* \approx 10^3$. The harmonic comb is the signature of a periodic signal of one fundamental frequency which conveys that the velocity field oscillates as a clean limit cycle and the harmonics are introduced by the nonlinear coupling between the momentum and energy equations. P9 carries the same fundamental at $f^* \approx 182$, recovered to within 1% of the P3 value, confirming that the entire side wall jet is locked to the plume oscillation at this Rayleigh number. The picture at P11 is different. Its

main peak sits at $f^* \approx 366$, which is the first harmonic, not the fundamental, and the spectrum then falls by more than three orders of magnitude across the same frequency window. The lower stratified pool therefore registers only the symmetric part of the plume oscillation; the cylinder filters out the asymmetric part before it can reach the bottom of the cavity. The integrated power at P11 is 1.0×10^4 in the units used, only about 11% of the P3 value, which matches the visual impression that the bottom of the cavity is nearly still at this Rayleigh number.

At $Ra = 10^7$ (Figure 20, 10^7 row) the broad shape of the spectrum is the same, but the harmonic comb has lost its sharpness. The dominant peak at P3 has moved to $f^* \approx 366$, and a second peak shows up at $f^* \approx 549$. The ratio of the two, $f_2/f_1 \approx 1.50$ which is irrational to the precision available. A weaker peak at $f^* \approx 915$ corresponds to the sum of the two. The simultaneous presence of two incommensurate frequencies and their combination tones is the spectral signature of a quasi-periodic state on a two torus, and not of a noisier periodic state: a noisy periodic signal would broaden each harmonic of a single fundamental but would not introduce new sharp peaks at incommensurate frequencies. The same two frequencies are recovered at P9 within the spectral resolution and the side wall jet is therefore still phase locked to the plume. At P11, by contrast, the spectrum has lost the clean peak at twice the fundamental that was present at $Ra = 7.5 \times 10^6$ and has developed a small but visible continuous floor between $f^* \approx 20$ and $f^* \approx 500$. The lower pool has therefore begun to register the second frequency introduced at the plume, although the response is still very weak.

By $Ra = 2.5 \times 10^7$ (Figure 20, $Ra = 2.5 \times 10^7$ row) the discrete peaks at P3 sit on top of a continuous spectral floor that extends across more than three decades in f^*. The coexistence of sharp peaks and a continuous background is what is normally seen at the chaotic edge of a quasi-periodic state, where the torus has begun to lose smoothness without the discrete frequencies having yet vanished into the background. P9 carries the same structure but with the discrete peaks reduced relative to the floor, indicating that the side wall jet is more disordered than the plume itself. P11 has changed qualitatively from $Ra = 10^7$: the spectrum is now continuous up to the same cutoff and the integrated power has risen from 1.2×10^4 to about 1.6×10^4, with the bottom of the cavity now active across a broad range of timescales.

At $Ra = 5 \times 10^7$ (Figure 20, $Ra = 5 \times 10^7$ row) the discrete peaks at P3 have effectively disappeared into a smooth continuous spectrum. The integrated power has reached 5.4×10^5, more than six times the value at $Ra = 7.5 \times 10^6$. P9 carries the same broad spectrum scaled by about 0.4. P11 has changed the most. The integrated power has roughly doubled relative to $Ra = 7.5 \times 10^6$ and the spectrum now extends two decades higher in frequency before rolling off, so the chaotic activity of the upper cavity has reached the bottom of the enclosure and is no longer filtered by the cylinder. The propagation of the disorder from the plume to the lower pool is therefore complete by the upper end of the Rayleigh number range studied here.

The dominant peak frequencies extracted from the four spectra at each of the three probes are given in Table 5, together with the integrated turbulent kinetic energy. The progression with Ra confirms three observations made above: (i) The fundamental frequency at the plume rises monotonically by a factor of about five between the lowest and the highest Rayleigh number, signalling a stiffer and faster oscillation as

Table 5: Dominant peak frequency f^*_{peak} of the energy spectral density and integrated turbulent kinetic energy E^* at the three retained probes, for the four post-critical Rayleigh numbers.

Ra	P3 (0.50, 0.95)		P9 (0.15, 0.50)		P11 (0.50, 0.15)	
	f^*_{peak}	E^*	f^*_{peak}	E^*	f^*_{peak}	E^*
7.5×10^6	183	8.77×10^4	182	3.40×10^4	366	1.00×10^4
10^7	366	1.20×10^5	366	4.79×10^4	336	1.18×10^4
2.5×10^7	549	2.65×10^5	458	9.93×10^4	458	1.62×10^4
5×10^7	961	5.44×10^5	763	2.13×10^5	763	2.03×10^4

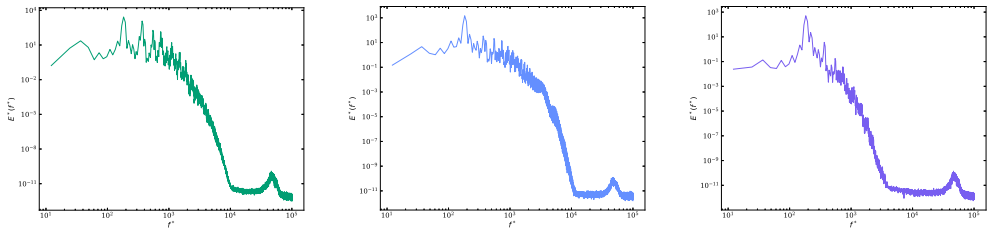
the boundary layers thin, (ii) The integrated power at P3 rises by a factor of about six over the same range, and (iii) The ratio E^*_{P11}/E^*_{P3} falls from 0.11 at $Ra = 7.5 \times 10^6$ to 0.04 at $Ra = 5 \times 10^7$, even though the absolute energy at P11 doubles. The cylinder absorbs an increasing fraction of the fluctuating energy injected by the side walls and only a small fraction reaches the bottom of the cavity, although the small fraction that does reach the bottom is itself broad band at the highest Rayleigh number.

5.4.5 Poincaré maps and phase space structure

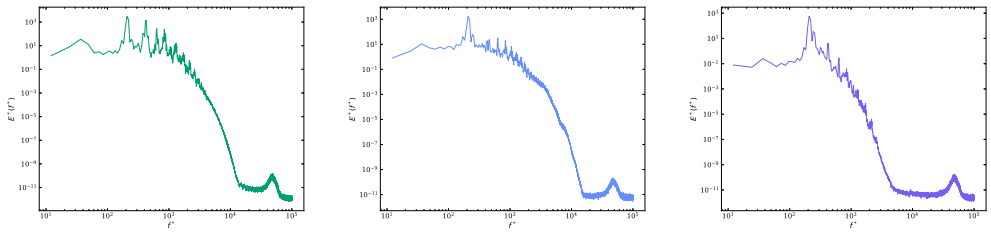
The energy spectral densities identify the regime of the velocity signal at each Rayleigh number but they do not show the geometry of the attractor that supports the dynamics. A clean limit cycle, a torus and a strange attractor produce a sharply peaked, a multi peaked and a broad band spectrum respectively, but the same three regimes also produce qualitatively different geometric objects in phase space, and it is the geometric object that is the more direct evidence of the route to chaos. This problem is resolved by discussing the phase plots of the velocity fluctuation in the (u', v') plane, and Poincaré maps obtained by recording v' at every upward zero crossing of u' at the same three probes P3, P9 and P11. The Poincaré section trades the continuous trajectory for a discrete set of points whose pattern is independent of the trajectory speed and is therefore the cleaner diagnostic when the trajectory becomes dense in phase space.

Throughout this subsection u' and v' denote the deviations of the horizontal and vertical velocity components from their time mean values at the corresponding probe. The time mean is removed because only the fluctuating dynamics are of interest in this study. The Poincaré maps plot the vertical fluctuation v' at the crossing against the change $\Delta v' = v'_{n+1} - v'_n$ between consecutive crossings. This format has the property that a periodic orbit projects to a small number of isolated points, a torus to a closed curve, and a strange attractor to a scattered cloud whose dimension is fractional.

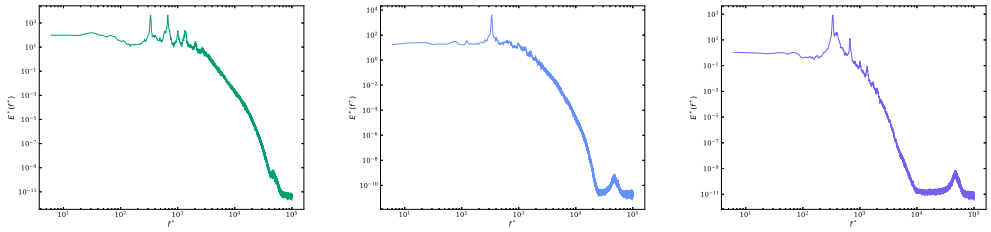
At $Ra = 7.5 \times 10^6$ (Figures 21 and 22, $Ra = 7.5 \times 10^6$ rows) the phase plot at P3 is a symmetric double-lobe limit cycle whose two halves are covered once per fundamental period. The lobes are sharp and the red and blue colours overlap cleanly, which means the cycle closes back on itself within the integration time used. The Poincaré section at the same probe consists of 108 crossings that sit on a smooth open arc, with a small total spread $\sigma_{\Delta v'} = 1.91$ (Table 6). A clean limit cycle would project to a single



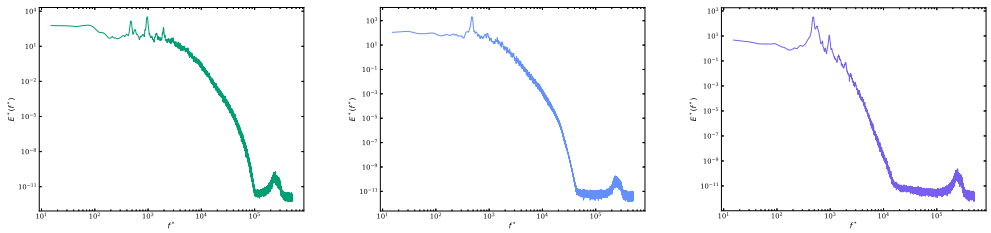
(a) P3, $Ra = 7.5 \times 10^6$ (b) P9, $Ra = 7.5 \times 10^6$ (c) P11, $Ra = 7.5 \times 10^6$



(d) P3, $Ra = 10^7$ (e) P9, $Ra = 10^7$ (f) P11, $Ra = 10^7$



(g) P3, $Ra = 2.5 \times 10^7$ (h) P9, $Ra = 2.5 \times 10^7$ (i) P11, $Ra = 2.5 \times 10^7$



(j) P3, $Ra = 5 \times 10^7$ (k) P9, $Ra = 5 \times 10^7$ (l) P11, $Ra = 5 \times 10^7$

Fig. 20: Energy spectral density of the velocity fluctuation vector $\mathbf{u}' = (u', v')$ at the three retained probes (columns: P3, P9, P11) and the four post critical Rayleigh numbers (rows).

point in this format. An arc instead of a point only means that the cycle, although periodic in the spectral sense, is not exactly closed in two dimensions: the projection onto (u', v') does not match the projection onto the dominant pair of phase-space coordinates. P9 carries a topologically equivalent attractor with the lobes rotated and elongated, and a Poincaré arc of similar smoothness with $\sigma_{\Delta v'} = 2.27$. The behaviour at P11 is different. Its phase plot is a single low-amplitude arch in the upper half-plane, with $|v'| \lesssim 25$ throughout, more than an order of magnitude smaller than the range seen at P3. The Poincaré section at P11 has 92 crossings with $\sigma_{\Delta v'} = 0.052$, so the lower stratified pool at this Rayleigh number behaves as a nearly still periodic background driven by the plume above.

At $Ra = 10^7$ (Figures 21 and 22, $Ra = 10^7$ rows) the phase plot at P3 has acquired a third lobe and the trajectory now visits a thickened, ribbon-like region rather than a one dimensional curve. The Poincaré section at P3 has expanded to 175 crossings with $\sigma_{\Delta v'} = 9.55$, a five-fold increase over $Ra = 7.5 \times 10^6$, and the points sit on a closed parabolic curve. A closed curve in the Poincaré plane is precisely the signature of a two torus in phase space. The second incommensurate frequency identified in the ESD has produced a second loop on the attractor, and the trajectory now wraps the torus densely without ever closing. P9 mirrors the same structure with the curve more elongated. P11 has departed from its nearly still state of the previous Rayleigh number. The phase plot has thickened to $|v'| \lesssim 60$ and the Poincaré section has 145 crossings with $\sigma_{\Delta v'} = 0.81$, sixteen times the value at $Ra = 7.5 \times 10^6$. The lower pool has therefore registered the onset of quasi-periodicity at the plume, although the absolute scale of the response is still small.

At $Ra = 2.5 \times 10^7$ (Figures 21 and 22, $Ra = 2.5 \times 10^7$ rows) the phase plot at P3 has lost the ribbon-like character of the previous case and is replaced by a dense, filled region with a clear inner core and a scattered halo of outliers. The boundary of the attractor is no longer a sharp curve. The Poincaré section at P3 contains 713 crossings with $\sigma_{\Delta v'} = 10.13$ and the points no longer fall on a closed curve. Instead they form a wedge shaped cloud with internal sub-structure, which is the visual hallmark of a strange attractor near the onset of chaos displaying a torus that has lost smoothness and developed a fractal cross section. P9 carries the same dense cloud at slightly lower amplitude with $\sigma_{\Delta v'} = 6.06$. P11 has changed the most relative to its $Ra = 10^7$ state: the Poincaré cloud is now 260 crossings wide and irregularly distributed with $\sigma_{\Delta v'} = 2.78$, so the lower pool now carries genuinely aperiodic activity, not merely the small response to a torus above it.

At $Ra = 5 \times 10^7$ (Figures 21 and 22, $Ra = 5 \times 10^7$ rows) the phase plot at P3 fills a large region of the (u', v') plane with no discernible internal structure beyond a slightly denser core, and the trajectory no longer revisits any well defined skeleton. The Poincaré section at P3 contains 485 crossings distributed as a broad cloud with $\sigma_{\Delta v'} = 9.32$, and the geometric distinction between periodic, quasi-periodic and chaotic states is now clearly resolved on the side of the chaotic state. The same is true at P9, whose cloud is somewhat narrower but otherwise topologically identical to P3. P11 has, by this Rayleigh number, also acquired a full Poincaré cloud with 198 crossings and $\sigma_{\Delta v'} = 0.20$ which in absolute terms the scatter at P11 remains two orders of

Table 6: Poincaré statistics at the three retained probes for the four post-critical Rayleigh numbers. N is the number of upward $u' = 0$ crossings in the analysis window and $\sigma_{\Delta v'}$ is the standard deviation of the vertical fluctuation increment between consecutive crossings.

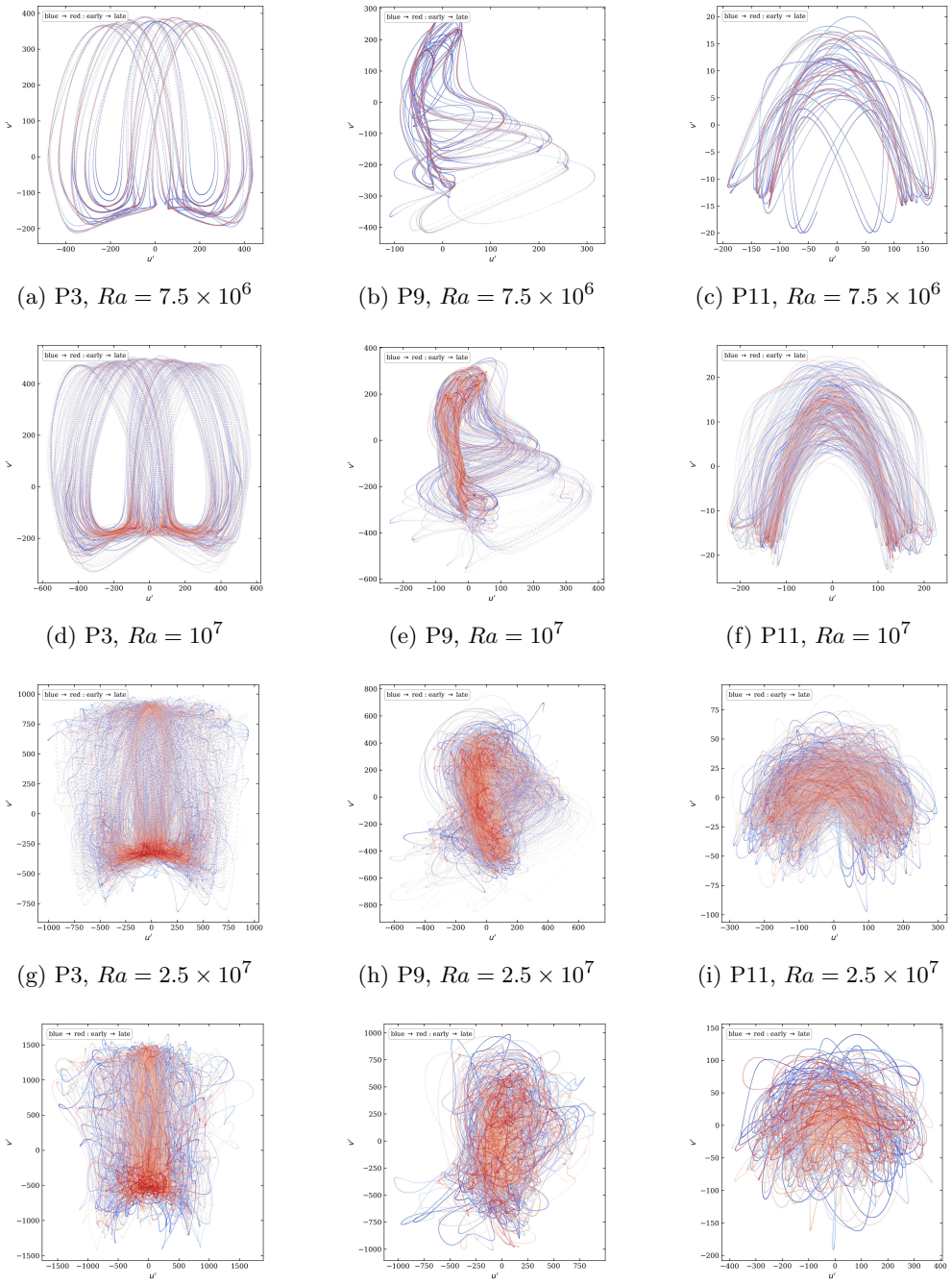
Ra	P3 (0.50, 0.95)		P9 (0.15, 0.50)		P11 (0.50, 0.15)	
	N	$\sigma_{\Delta v'}$	N	$\sigma_{\Delta v'}$	N	$\sigma_{\Delta v'}$
7.5×10^6	108	1.91	101	2.27	92	0.052
10^7	175	9.55	148	1.91	145	0.81
2.5×10^7	713	10.13	310	6.06	260	2.78
5×10^7	485	9.32	260	1.29	198	0.20

magnitude smaller than at P3, but the cloud has no remaining structure, and the bottom of the cavity is no longer protected from the chaotic forcing of the plume above.

If the evolution is taken in sequence, Figures 21 and 22 resolve the route from periodicity to chaos in this geometry as a Ruelle-Takens-Newhouse scenario [33, 39] rather than a period doubling cascade or an intermittency route. The signature of the Ruelle-Takens-Newhouse route is precisely the sequence limit cycle (Figs. 21a and 22a) $\rightarrow$ two torus (Figs. 21d and 22d) $\rightarrow$ strange attractor (Figs. 21j and 22j) that is recovered here in three steps as the Rayleigh number rises from 7.5×10^6 to 5×10^7, with the second frequency appearing through a Hopf-like secondary instability between $Ra = 7.5 \times 10^6$ and $Ra = 10^7$ and the torus losing smoothness between $Ra = 10^7$ and $Ra = 2.5 \times 10^7$ (Figs. 21g and 22g). The Poincaré standard deviation $\sigma_{\Delta v'}$ at the three probes, given in Table 6, gives a numerical footprint of this sequence and of how it spreads through the cavity. At the plume probe P3, $\sigma_{\Delta v'}$ grows by a factor of about five at the first transition (limit cycle to torus), stays at a similar level through the second (torus to chaos), and then drops back slightly as the chaotic state settles in. At the bottom probe P11, by contrast, $\sigma_{\Delta v'}$ rises by a factor of about 15 between $Ra = 7.5 \times 10^6$ and $Ra = 10^7$, by a further factor of 3.4 between $Ra = 10^7$ and $Ra = 2.5 \times 10^7$, and stays roughly constant thereafter. The delayed and progressive response of P11 confirms the interpretation given in the spectral analysis. The disorder is generated at the plume above the cylinder, propagates down the side walls through the descending jet, and only fills the lower stratified pool at the upper end of the Rayleigh number range studied here.

6 Conclusion

A time accurate finite element study has been carried out for buoyancy driven flow of air ($Pr = 0.71$) inside a cold square cavity with a heated circular cylinder of radius $R = 0.2L$ at its geometric centre. Eight Rayleigh numbers spanning $10^4 \leq Ra \leq 5 \times 10^7$ were studied on a body conforming mesh, retaining the unsteady terms and imposing no symmetry condition on the vertical centre line, so that any asymmetric mode permitted by the physics is free to grow on its own. The solver was first validated against the differentially heated cavity benchmark of De Vahl Davis [14], and the GCI



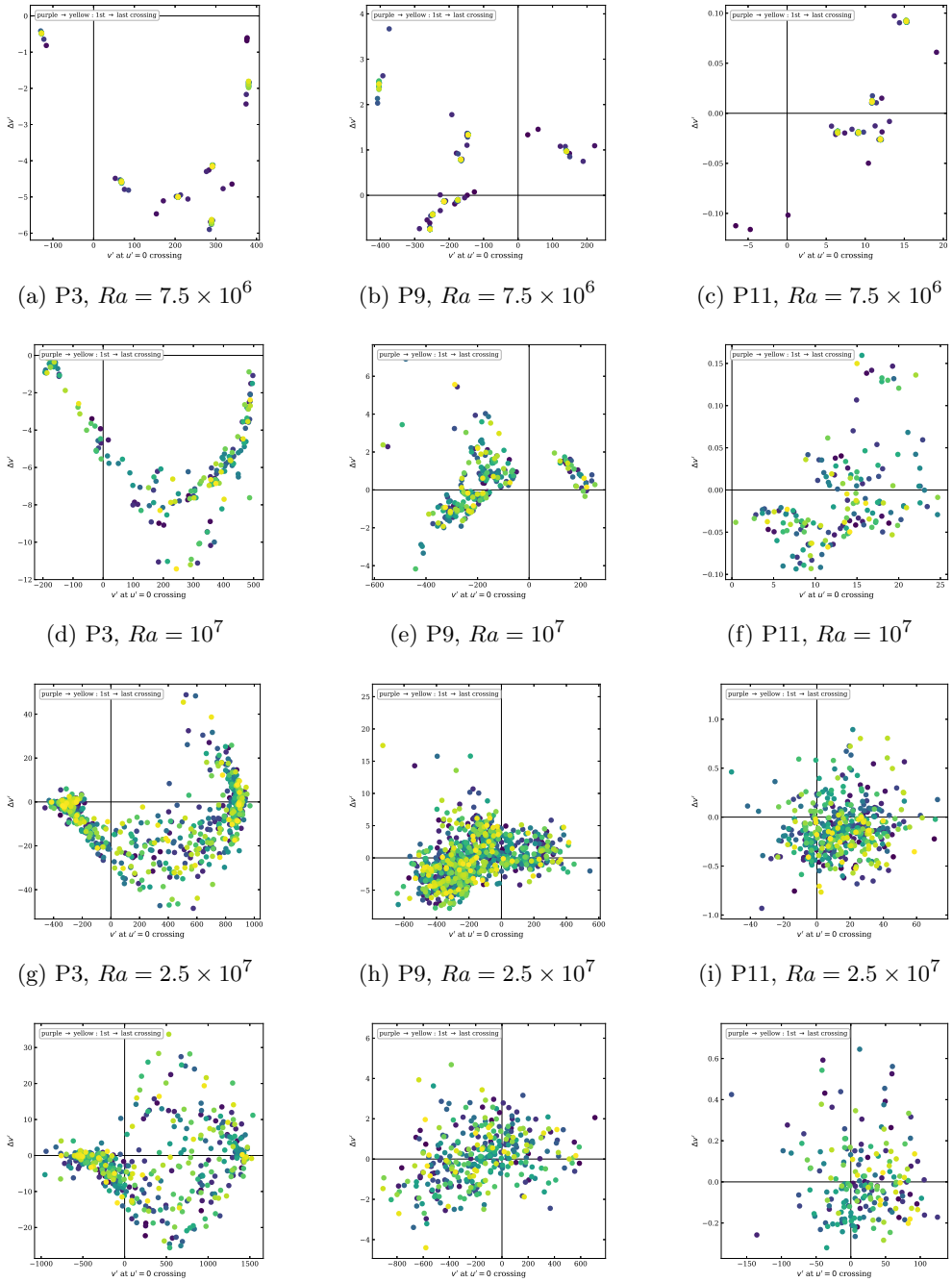
(a) P3, $Ra = 7.5 \times 10^6$ (b) P9, $Ra = 7.5 \times 10^6$ (c) P11, $Ra = 7.5 \times 10^6$

(d) P3, $Ra = 10^7$ (e) P9, $Ra = 10^7$ (f) P11, $Ra = 10^7$

(g) P3, $Ra = 2.5 \times 10^7$ (h) P9, $Ra = 2.5 \times 10^7$ (i) P11, $Ra = 2.5 \times 10^7$

(j) P3, $Ra = 5 \times 10^7$ (k) P9, $Ra = 5 \times 10^7$ (l) P11, $Ra = 5 \times 10^7$

Fig. 21: Phase plots of the velocity fluctuation in the (u', v') plane at the three retained probes (columns: P3, P9, P11) and the four post critical Rayleigh numbers (rows).



(a) P3, $Ra = 7.5 \times 10^6$ (b) P9, $Ra = 7.5 \times 10^6$ (c) P11, $Ra = 7.5 \times 10^6$

(d) P3, $Ra = 10^7$ (e) P9, $Ra = 10^7$ (f) P11, $Ra = 10^7$

(g) P3, $Ra = 2.5 \times 10^7$ (h) P9, $Ra = 2.5 \times 10^7$ (i) P11, $Ra = 2.5 \times 10^7$

(j) P3, $Ra = 5 \times 10^7$ (k) P9, $Ra = 5 \times 10^7$ (l) P11, $Ra = 5 \times 10^7$

Fig. 22: Poincaré sections at upward $u' = 0$ crossings of the probe signal for the three retained probes (columns: P3, P9, P11) and the four post critical Rayleigh numbers (rows).

study returned a fine grid uncertainty of 0.84% on $\overline{Nu}_{\mathrm{cyl}}$. As the Rayleigh number was increased, the flow passed through three distinct regimes, steady, quasi periodic and chaotic, and the present study brackets the critical Rayleigh number that separates them and traces the full sequence of states in between.

Up to $Ra \approx 5\times10^6$ the flow remains steady and symmetric about the vertical centre line, with two mirror image recirculation cells around the cylinder and a single thermal plume rising from the cylinder cap to the cold top wall. The first trace of symmetry breaking already appears at $Ra = 5 \times 10^6$, where the negative stream function core $|\psi_{\min}| = 35.87$ exceeds the positive core $\psi_{\max} = 34.61$ by about 3.6%, even though the contours still look mirror symmetric to the eye. Tracking the standard deviation of the cylinder averaged Nusselt number $Nu_{\mathrm{cyl}}(t)$ across all eight cases then locates the onset of unsteadiness in the band $5 \times 10^6 < Ra_{\mathrm{c}} < 7.5 \times 10^6$, Eqn. (45), where $\sigma(Nu_{\mathrm{cyl}})$ jumps by more than three orders of magnitude for a Rayleigh number ratio of only 1.5. Since the present formulation does not clamp the cylinder stream function to zero, this critical value comes out higher than the one implied by the steady only computation of Dutta et al. [17], in which the enforced symmetry suppresses the very mode that drives the transition.

Past Ra_{c} the flow proceeds to chaos along the Ruelle-Takens-Newhouse route [33, 39]. The energy spectral densities and the Poincaré sections recorded at the eleven probes together establish a clean limit cycle at $Ra = 7.5 \times 10^6$, a quasi periodic state on a two torus at $Ra = 10^7$ once a second incommensurate frequency sets in, and a broad band strange attractor at $Ra = 5 \times 10^7$, the torus losing its smoothness in between. The disorder is not produced everywhere at once; it is born in the thermal plume above the cylinder and is carried downward by the descending side wall jets, while the lower stratified pool stays nearly quiet until the highest Rayleigh number. This staged spreading shows up in the probe energy ratio E^*_{P11}/E^*_{P3}, which falls from 0.11 at $Ra = 7.5 \times 10^6$ to 0.04 at $Ra = 5 \times 10^7$, the bottom of the cavity turning broad band only at the upper end of the range. It is worth noting that although every instantaneous snapshot in this regime is strongly asymmetric, the long time averaged fields recover the bilateral symmetry of the steady solution. This is a statistical effect: the reflection symmetry of the equations and boundary conditions makes the mirror image of every visited state equally admissible, so the average settles on the symmetry plane, and the near steady look of the mean fields should not be mistaken for a steady flow.

The heat transfer results tie the whole range together. A single power law $\overline{Nu}_{\mathrm{cyl}} = 0.764\, Ra^{0.226}$, Eqn. (46), fits all eight time averaged cylinder Nusselt numbers, steady and unsteady, to within 6%. Fitted on their own the steady and unsteady branches give $n = 0.224$ and $n = 0.243$ respectively, both lying between the laminar boundary layer value $n = 1/4$ [7] and the Castaing soft turbulence scaling $n = 2/7 \approx 0.286$ [10], which places the flow between a boundary layer controlled state and fully developed turbulence. The partition of heat among the walls stays almost unchanged across the range, the top wall absorbing close to 55% and each side wall about 22%, while the bottom wall accounts for less than 2%. The bottom wall in fact behaves counter intuitively, its averaged Nusselt number $\overline{Nu}_{\mathrm{bot}}$ *decreasing* with Ra, because the strengthening stratification and the bottom corner eddies keep the cold side wall jets away from the lower

boundary layer. The peak cylinder heat flux stays pinned at $\theta_{\text{peak}} = 275.35°$ for every case except $Ra = 5 \times 10^7$, where it shifts to 243.07° under the long lived asymmetric plume configurations of the chaotic state.

These results supply reference data on the critical Rayleigh number, the regime sequence, and the global heat transfer correlation that earlier steady-only studies could not provide. The study is, however, restricted to a two dimensional cavity, a single cylinder of radius $R = 0.2L$ fixed at the centre, and one Prandtl number. Extensions of the present body conforming solver to three dimensional flow, to off centre and different sized cylinders, and to higher Prandtl numbers are natural directions for future work.

Acknowledgements. Not applicable.

Declarations

Funding. The authors declare that no funds, grants, or other support were received during the preparation of this manuscript.

Competing interests. The authors declare no competing interests.

Author contributions. Mannu Yadav: Conceptualization, Methodology, Software, Validation, Formal analysis, Investigation, Writing – original draft. Anil Lal Sadasivan: Conceptualization, Supervision, Writing – review & editing.

Data availability. The data that support the findings of this study are available from the corresponding author upon reasonable request.

Code availability. The in-house FORTRAN solver used in this study is available from the corresponding author upon reasonable request.

References

[1] A. Xu LS, Zhao T (2017) Accelerated lattice boltzmann simulation using gpu and openacc with data management. International Journal of Heat and Mass Transfer 109:577–588. https://doi.org/https://doi.org/10.1016/j.ijheatmasstransfer.2017.02.032

[2] Ait-Taleb A, Abdelbaki A, Zrikem Z (2016) Numerical study of natural convection in a square cavity with an inner heated circular cylinder. International Journal of Heat and Technology 34(3):377–384. https://doi.org/10.18280/ijht.340305

[3] Ascher UM, Ruuth SJ, Wetton BTR (1995) Implicit-explicit methods for time-dependent partial differential equations. SIAM Journal on Numerical Analysis 32(3):797–823. https://doi.org/10.1137/0732037

[4] Barrett R, Berry M, Chan TF, et al (1994) Templates for the Solution of Linear Systems: Building Blocks for Iterative Methods, 2nd edn. SIAM, Philadelphia, PA, https://doi.org/10.1137/1.9781611971538

[5] Basak T, Roy S, Pop I (2009) Finite element analysis of natural convection in a square cavity. International Journal of Heat and Mass Transfer 52(7–8):1706–1720

[6] Bathe KJ (1996) Finite Element Procedures. Prentice-Hall, Englewood Cliffs, NJ

[7] Bejan A (2013) Convection Heat Transfer, 4th edn. Wiley

[8] Canuto C, Hussaini MY, Quarteroni A, et al (1988) Spectral Methods in Fluid Dynamics. Springer, Berlin

[9] Carey GF, Oden JT (1986) Finite Elements: Fluid Mechanics. Prentice-Hall, Englewood Cliffs, NJ

[10] Castaing B, Gunaratne G, Heslot F, et al (1989) Scaling of hard thermal turbulence in Rayleigh–Bénard convection. Journal of Fluid Mechanics 204:1–30. https://doi.org/10.1017/S0022112089001643

[11] Celik IB, Ghia U, Roache PJ, et al (2008) Procedure for estimation and reporting of uncertainty due to discretization in CFD applications. Journal of Fluids Engineering 130(7):078001. https://doi.org/10.1115/1.2960953

[12] Chenoweth DR, Paolucci S (1986) Natural convection in an enclosed vertical air layer with large horizontal temperature differences. Journal of Fluid Mechanics 169:173–210. https://doi.org/10.1017/S0022112086000587

[13] Chorin AJ (1968) Numerical solution of the Navier–Stokes equations. Mathematics of Computation 22(104):745–762. https://doi.org/10.1090/S0025-5718-1968-0242392-2

[14] De Vahl Davis G (1983) Natural convection of air in a square cavity: A bench-mark numerical solution. International Journal for Numerical Methods in Fluids 3(3):249–264. https://doi.org/10.1002/fld.1650030305

[15] Demirdžić I, Lilek v, Perić M (1992) Fluid flow and heat transfer test problems for non-orthogonal grids: bench-mark solutions. International Journal for Numerical Methods in Fluids 15(3):329–354. https://doi.org/10.1002/fld.1650150306

[16] Donea J, Huerta A (2003) Finite Element Methods for Flow Problems. Wiley, Chichester

[17] Dutta S, Kumar P, Kalita JC (2020) Streamfunction–vorticity computation of natural convection around a heated circular cylinder placed inside a square enclosure. International Journal of Heat and Mass Transfer 152:119550. https://doi.org/10.1016/j.ijheatmasstransfer.2020.119550

[18] Ferziger JH, Perić M (2002) Computational Methods for Fluid Dynamics, 3rd edn. Springer, Berlin

[19] Guermond JL, Minev P, Shen J (2006) An overview of projection methods for incompressible flows. Computer Methods in Applied Mechanics and Engineering 195(44–47):6011–6045. https://doi.org/10.1016/j.cma.2005.10.010

[20] Holman JP (2010) Heat Transfer, 10th edn. McGraw-Hill

[21] Hortmann M, Perić M, Scheuerer G (1990) Finite volume multigrid prediction of laminar natural convection. International Journal for Numerical Methods in Fluids 11(2):189–207. https://doi.org/10.1002/fld.1650110206

[22] Hughes TJR (2000) The Finite Element Method: Linear Static and Dynamic Finite Element Analysis. Dover Publications, Mineola, NY

[23] Hughes TJR, Winget J, Levit I, et al (1983) New alternating direction procedures in finite element analysis based upon EBE approximate factorizations. Computer Methods in Applied Mechanics and Engineering 56(1):43–73. https://doi.org/10.1016/0045-7825(83)90117-9

[24] Incropera FP, DeWitt DP, Bergman TL, et al (2011) Fundamentals of Heat and Mass Transfer, 7th edn. Wiley

[25] Kalita JC, Dalal DC, Dass AK (2001) Fully compact higher-order computation of steady-state natural convection in a square cavity. Phys Rev E 64:066703. https://doi.org/10.1103/PhysRevE.64.066703

[26] Kim BS, Hyun JM (2016) Natural convection in a square enclosure with a circular cylinder. International Journal of Heat and Fluid Flow 61:387–399

[27] Kim BS, Lee DS, Ha MY, et al (2008) Natural convection in a square enclosure with a circular cylinder at different vertical locations. International Journal of Heat and Mass Transfer 51(7–8):1888–1906. https://doi.org/10.1016/j.ijheatmasstransfer.2007.06.033

[28] Lal SA, Jabir E (2010) A hybrid finite element—finite volume method for incompressible flow through complex geometries using mixed grids. Proceedings of the Institution of Mechanical Engineers, Part G: Journal of Aerospace Engineering 224(1):23–41. https://doi.org/10.1243/09544100JAERO598

[29] Lal SA, Kumar VA (2013) Numerical prediction of natural convection in a vertical annulus closed at top and opened at bottom. Heat Transfer Engineering 34(1):70–83. https://doi.org/10.1080/01457632.2013.714441

[30] Le Quéré P (1991) Accurate solutions to the square natural convection benchmark problem. International Journal of Heat and Fluid Flow 12(3):221–234

[31] Mahmoodi M (2011) Natural convection in a square cavity with an internal cylinder. International Communications in Heat and Mass Transfer 38:462–467

[32] Moukalled F, Acharya S (1996) Natural convection in the annulus between concentric horizontal circular and square cylinders. Journal of Thermophysics and Heat Transfer 10(3):524–531. https://doi.org/10.2514/3.821

[33] Newhouse S, Ruelle D, Takens F (1978) Occurrence of strange Axiom A attractors near quasi periodic flows on t^m, $m \geq 3$. Communications in Mathematical Physics 64(1):35–40

[34] OpenMP Architecture Review Board (2018) OpenMP application programming interface, version 5.0. Tech. rep., OpenMP ARB, URL https://www.openmp.org/specifications/

[35] Oztop HF, Abu-Nada E (2008) Numerical study of natural convection in partially heated enclosures. International Journal of Heat and Fluid Flow 29:1326–1336. https://doi.org/10.1016/j.ijheatfluidflow.2008.04.009

[36] Patankar SV (1980) Numerical Heat Transfer and Fluid Flow. Hemisphere

[37] Richardson LF (1911) The approximate arithmetical solution by finite differences of physical problems involving differential equations, with an application to the stresses in a masonry dam. Philosophical Transactions of the Royal Society A 210:307–357. https://doi.org/10.1098/rsta.1911.0009

[38] Roache PJ (1998) Verification and Validation in Computational Science and Engineering. Hermosa Publishers, Albuquerque, NM

[39] Ruelle D, Takens F (1971) On the nature of turbulence. Communications in Mathematical Physics 20(3):167–192

[40] Saad Y (2003) Iterative Methods for Sparse Linear Systems, 2nd edn. SIAM, Philadelphia, PA, https://doi.org/10.1137/1.9780898718003

[41] Sheikholeslami M, Gorji-Bandpy M, Ganji DD (2012) Lattice boltzmann simulation of natural convection in cavities. International Journal of Heat and Mass Transfer 55(13–14):3978–3988

[42] Shu C, Xue H, Zhu YD (2001) Numerical study of natural convection in an eccentric annulus between a square outer cylinder and a circular inner cylinder using DQ method. International Journal of Heat and Mass Transfer 44(17):3321–3333. https://doi.org/10.1016/S0017-9310(00)00357-4

[43] Sun H, Pop I, Ingham DB (2014) Natural convection around a heated cylinder in an enclosure. International Journal of Heat and Mass Transfer 72:646–655

[44] Temam R (1969) Sur l'approximation de la solution des équations de Navier–Stokes par la méthode des pas fractionnaires (II). Archive for Rational Mechanics and Analysis 33(5):377–385. https://doi.org/10.1007/BF00247696

[45] Trias FX, Gorobets A, Soria M, et al (2010) Direct numerical simulation of turbulent natural convection. Physics of Fluids 22:055103

[46] Versteegh TAM, Nieuwstadt FTM (1998) Turbulent natural convection in a square cavity. Journal of Fluid Mechanics 370:25–59

[47] Wang Y, Chen Z, Liu M (2017) Unsteady natural convection in a cavity with a heated cylinder. International Journal of Heat and Mass Transfer 108:2106–2118

[48] Yu P, Tian ZF (2013) A compact streamfunction–velocity scheme on nonuniform grids for the 2d steady incompressible navier–stokes equations. Computers & Mathematics with Applications 66(7):1192–1212. https://doi.org/https://doi.org/10.1016/j.camwa.2013.07.013

[49] Zienkiewicz OC, Zhu JZ (1992) The superconvergent patch recovery and a posteriori error estimates. Part 1: The recovery technique. International Journal for Numerical Methods in Engineering 33(7):1331–1364. https://doi.org/10.1002/nme.1620330702

[50] Zienkiewicz OC, Taylor RL, Zhu JZ (2005) The Finite Element Method: Its Basis and Fundamentals, 6th edn. Elsevier Butterworth-Heinemann, Oxford